Probing the Properties of the Molecular Adlayers on Metal Substrates:

Scanning Tunneling Microscopy Study of Amine Adsorption on Au(111) and Graphene Nanoislands on Co(0001)

Hui Zhou

Submitted in partial fulfillment of the

requirements for the degree of

Doctor of Philosophy

in the Graduate School of Arts and Science

COLUMBIA UNIVERSITY

2011

Abstract

Probing the Properties of the Molecular Adlayers on Metal Substrates:

Scanning Tunneling Microscopy Study of Amine Adsorption on Au(111) and Graphene Nanoislands on Co(0001)

Hui Zhou

In this thesis, we present our findings on two major topics, both of which are studies of molecules on metal surfaces by scanning tunneling microscopy (STM).

The first topic is on adsorption of a model amine compound, 1,4-benzenediamine (BDA), on the reconstructed Au(111) surface, chosen for its potential application as a molecular electronic device. The molecules were deposited in the gas phase onto the substrate in the vacuum chamber. Five different patterns of BDA molecules on the surface at different coverages, and the preferred adsorption sites of BDA molecules on reconstructed Au(111) surface, were observed. In addition, BDA molecules were susceptible to tip-induced movement, suggesting that BDA molecules on metal surfaces can be a potential candidate in STM molecular manipulations.

We also studied graphene nanoislands on Co(0001) in the hope of understanding interaction of expitaxially grown graphene and metal substrates. This topic can shed a light on the potential application of graphene as an electronic device, especially in spintronics. The graphene nanoislands were formed by annealing contorted

hexabenzocoronene (HBC) on the Co(0001) surface. In our experiments, we have determined atop registry of graphene atoms with respect to the underlying Co surface. We also investigated the low-energy electronic structures of graphene nanoislands by scanning tunneling spectroscopy. The result was compared with a first-principle calculation using density functional theory (DFT) which suggested strong coupling between graphene π-bands and cobalt d-electrons. We also observed that the islands exhibit zigzag edges, which exhibits unique electronic structures compared with the center areas of the islands.

Contents

List of Tables

List of Figures

Acknowledgement

Seven years. Looking back, I found the journey as the most demanding task in my life. I was lucky to have so many people's hands on my way to the mountain top. Without them, I don't think I would have finally made it.

I owe my greatest gratitude to my advisor, Tony Heinz. He has been a guiding landmark along the whole way, from the moment he admitted me to Columbia University to the moment he saw me leave after defense. He not only set an example of hard-working, but also showed the greatest patience with his students. Moreover, I would not been able to find my life path without his encouragement and help during my final year as a student.

I also want to thank my husband, Dr. Jie Lin, for his biggest heart and support for whatever decision I make. He is my emotional pillow and he is always there for me.

There are two people who taught me the most in experiment techniques. Dr. Daejin Eom opened the door of STM to me and provided a continuous help with my experiment. Dr. Zonghai Hu, whom I still owe a paper, showed selfless devotion into my project.

I am also grateful to a lot of other professors and colleagues in research. Prof. Flynn, who has been my unofficial advisor in the Chemistry Department, provided a great sight

and continuous support for my project. Prof. Morgante taught me a lot of vaccum techniques and helped me settle down on my trip to Italy. Prof. Venkataramen and her student, Masha Kamenetska, along with Prof. Morgante' student, Dr. Martina Dell'angela filled me in with knowledge of benzenediamine. Dr. Kwang Taeg Rim set a good example of consistency in research and his optimism often encouraged me. Prof. Abhay Pasupathy often provided me some insightful discussions. Liuyan Zhao has been a best friend and a great inspiration inside and outside of the lab.

I wish to thank the following teachers and colleagues for their wisdom and expertise: Prof. Andrew Millis, Dr. Li Liu, Dr. Hao Wang, Dr. Hayn Park, Dr. Hugen Yan, Dr. Yang Wu, Dr. Daohua Song, Dr. Joanna Atkin, Dr. Kin Fai Mak, Dr. Joshua Lui, Dr. Sami Rosenblatt, Dr.G ina Florio, Dr. Mingyuan Huang and Dr. Scott Goncher.

Looking back, I realized that there are so many people I owe gratitude to. Thanks to all of them, my seven years become so precious. I will take the attitude and skills they taught me and continue my life journey.

Chapter 1

Introduction to STM and Applications of STM

The Scanning Tunneling Microscope (STM) was invented by Binnig and Rohrer in 1981 who shared the 1986 Nobel Prize in Physics[6]. It is a powerful instrument to image surfaces at the atomic level, achieving a lateral resolution of 0.1nm and vertical resolution of 0.01nm[12]. At this scale, individual atoms on the material surfaces can be resolved. In this chapter, I will review the principles of the STM and its applications, focusing on Scanning Tunneling Spectroscopy (STS) and atom/molecule manipulation with STM.

1.1. Principle of the STM

1.1.1. The Concept of Tunneling

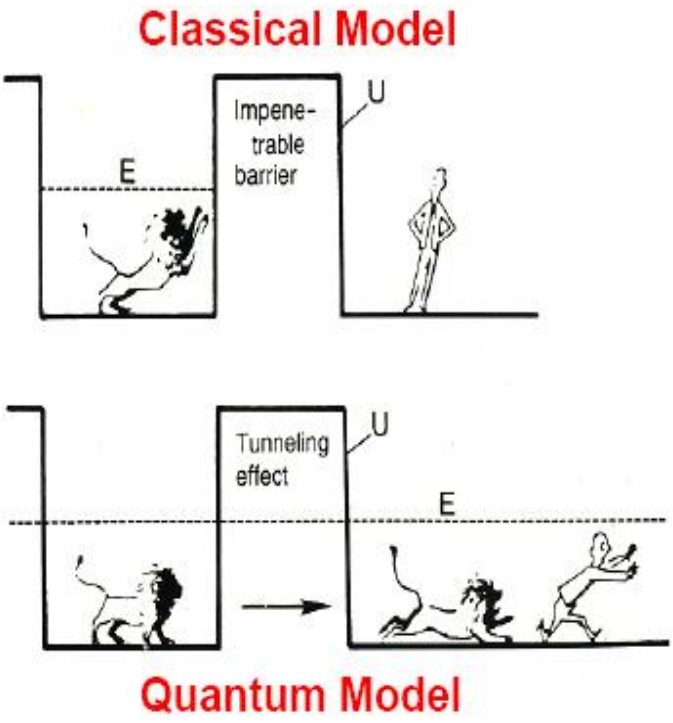

Figure 1.1 The difference between classical theory and quantum theory.

When U>E , in classical mechanics, the electron cannot overcome a barrier; in quantum mechanics, the electron has a non-zero probability to tunnel through the barrier [2] .

The operation of the STM is based on the phenomenon of quantum mechanical tunneling. Imagine a potential barrier and a microscopic particle, e.g. an electron, with energy smaller than the potential barrier, as illustrated in Figure 1.1. In classical mechanics, the electron is confined by the barrier region; while in quantum mechanics,

the electron can tunnel through the barrier. To illustrate the tunneling, we consider a simplified one-dimensional model shown in Figure 1.2. In this case, the electron is described by a wavefunction $\psi(x)$, which satisfies the one-dimensional Schrödinger Equation.

$$-\frac{\hbar^2}{2m}\frac{\partial^2\psi(x)}{\partial x^2}+U(x)\psi(x)=E\psi(x) \quad (1.1)$$

Its solution in the classical forbidden region is:

$$\psi(x)=\psi(0)e^{-\kappa x}, \quad (1.2)$$

where

$$\kappa=\frac{\sqrt{2m(U-E)}}{\hbar} \quad (1.3)$$

is the decay constant. Thus, the probability density through the barrier is proportional to $|\psi(L)|^2=|\psi(0)|e^{-2\kappa L}$, where L is the barrier width. Here we define a transmission coefficient T, as the ratio of the transmitted current density and the incident current density[10]. In a simplified junction with equal potentials on the tip and sample In Figure 1.2b, T is given as:

$$T=\frac{I(x)}{I(0)}\propto e^{-2\kappa x} \quad (1.4)$$

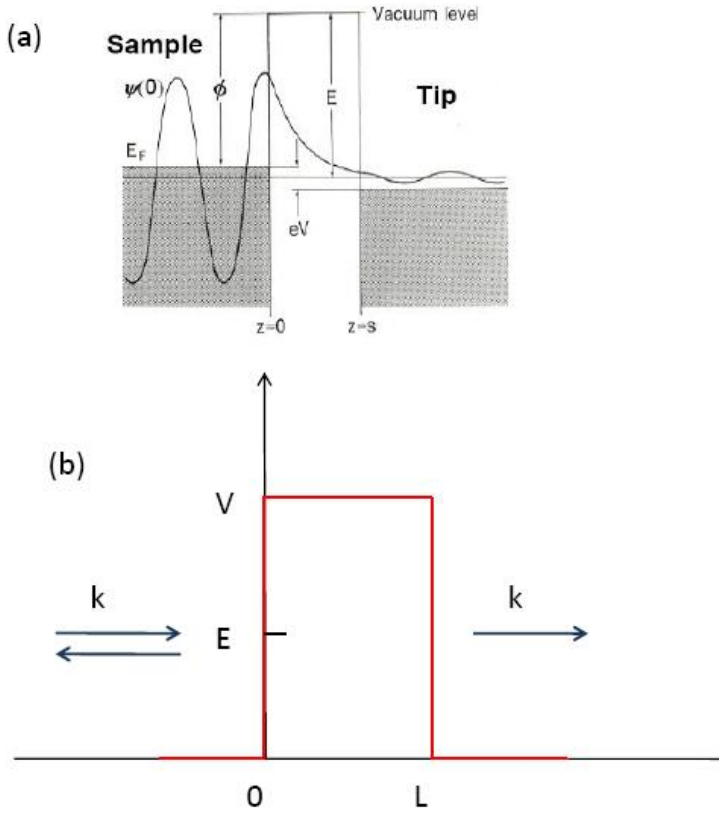

Figure 1.2: A one-dimensional metal-vacuum-metal tunneling junction.

(a) Electrons can tunnel through vacuum (modeled with a potential barrier) between the sample and the tip with a decayed wavefunction[2]. (b) A simplified one-dimension model with equal potentials on both ends and a square potential barrier.

A typical value for $1/\kappa$ is about 0.1nm. Thus, according to Eq 1.4, the current decays about 10 times, or one order of magnitude, when the tip-sample distance changes by about 0.1nm. This gives STM spatial sensitivity on the atomic scale.

In 1957, a more quantitative study was provided by Landauer[13] who used the semiclassical WKB approximation to calculate the tunneling probability. It has two important assumptions: First, the electrodes can be described by a one-dimensional free-electron gas in an ideal square potential well. Second, the current is ballistic, which means the current is the product of the density of the electron and the classical velocity in the electrodes. When no bias voltage is applied, the electrons from either the sample or the tip have equal tunneling probability to the other side through the vacuum which leads to zero net tunneling current. When a negative sample bias is applied, a difference of the Fermi levels of two electrodes is generated and a net current flows. As a result, we observe a single-channel current of:

$$I_t = \frac{2e^2}{h} VT \quad , \tag{1.5}$$

where T is the tunneling coefficient, which can be calculated in the WKB approximation. The tunneling conductance G is defined as:

$$G \equiv \frac{I_t}{V} = \frac{2e^2}{h} T \equiv G_0 T \quad , \tag{1.6}$$

where the conductance quantum G_0 is given by:

$$G_0 = \frac{2e^2}{h} \approx 77.48 \mu S \quad . \tag{1.7}$$

If we assume the vacuum can be approximated by a square potential barrier, then $T \propto e^{-2\kappa x}$, and

$$G \propto G_0 e^{-2\kappa x}. \tag{1.8}$$

In practice, the transmission coefficient T is complicated by the tip geometry and the surface electronic structure[8, 9]. But the general tendency of $T \propto e^{-2\kappa x}$ remains the same.

1.1.2. The Theory of STM

One widely used theory for the tunneling phenomenon in solids, as well as in STM is Bardeen Tunneling Theory. Bardeen first introduced the following tunneling approximation[14]:

$$I = \frac{2\pi e}{\hbar} \sum_{\mu,\nu} f(E_\mu)[1 - f(E_\nu + eV)] |M_{\mu\nu}|^2 \, \delta(E_\mu - E_\nu), \tag{1.9}$$

where f(E) is the Fermi distribution function, V is the applied voltage, and $M_{\mu\nu}$ is the tunneling matrix element between the states of the probe and those of the surface (μ denotes a state of one electrode and ν denotes a state of the other). Note that the reference point of zero energy is the Fermi level. $M_{\mu\nu}$ is given by

$$M_{\mu\nu} = \frac{\hbar^2}{2m} \int d\mathrm{S} \cdot (\psi_\mu^* \nabla \psi_\nu - \psi_\nu \nabla \psi_\mu^*), \tag{1.10}$$

where E_μ and E_ν are the energies corresponding to ψ_μ and ψ_ν, respectively, and the integral is over the entire surface within the vacuum barrier region.

By introducing the density of states of both electrodes, Eq 1.9 can be rewritten as:

$$I = \frac{4\pi e}{\hbar} \int_{-\infty}^{\infty} |M|^2 \rho_s(E)\rho_t(E-eV)[f(E-eV) - f(E)]dE \quad (1.11)$$

where s denotes the sample, and t denotes the tip. M is the tunneling matrix element defined in Equation 1.10. This equation indicates that *the tunneling currently is directly related to the local density of states (LDOS) of the surface at the Fermi level.*

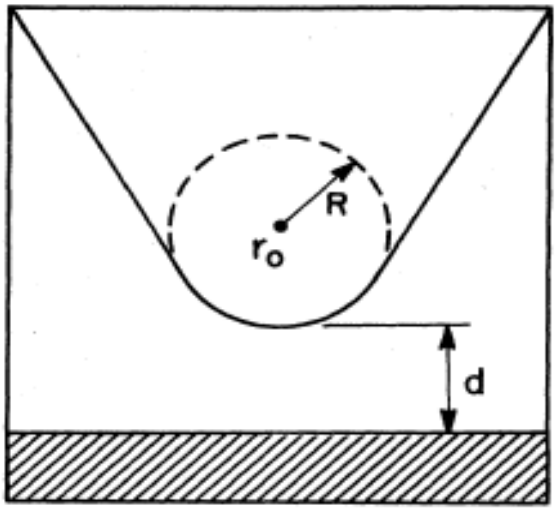

Figure 1.3 Schematic picture of tunneling junction in Tersoff and Hamann analysis[8, 9].

The tip is modeled as a spherical object with radius R and the center r_o. The tip and sample distance is d.

Later on, further refinements were made for the theory of STM. For example, Tersoff and Hamann[8, 9] modeled the tip with an s-wave approximation (μ) for a spherical

object and the surface with a general expansion of Bloch functions (ν) (See Fig. 1.3). They obtained the following simplified formula:

$$I = 32\pi^3\hbar^{-1}e^2V\phi^2D_t(E_F)R^2\kappa^{-4}e^{2\kappa R}\cdot\sum_{\nu}|\psi_\nu(r_0)|^2\ \delta(E_\nu - E_F), \qquad (1.12)$$

where D_t is the density of states per unit volume of the tip. Through these advances, STM theory can be applied towards the understanding of some experimental data.

1.2. The Introduction of STS

1.2.1. The Concept of STS

Lang[15] proposed the following picture at zero temperature (Fig 1.4). At zero bias, the Fermi levels of the sample and tip are equal. When a positive sample bias is applied, a net tunneling current arises from tunneling electrons from the occupied states of the tip to the unoccupied states of the surface, whereas when a negative sample bias applied, there is a net current tunnel from occupied states of the sample into unoccupied states of the tip. As a result, the polarity of the sample bias determines whether the occupied states or the unoccupied states of the sample are probed. This is the idea of Scanning Tunneling Spectroscopy (STS).

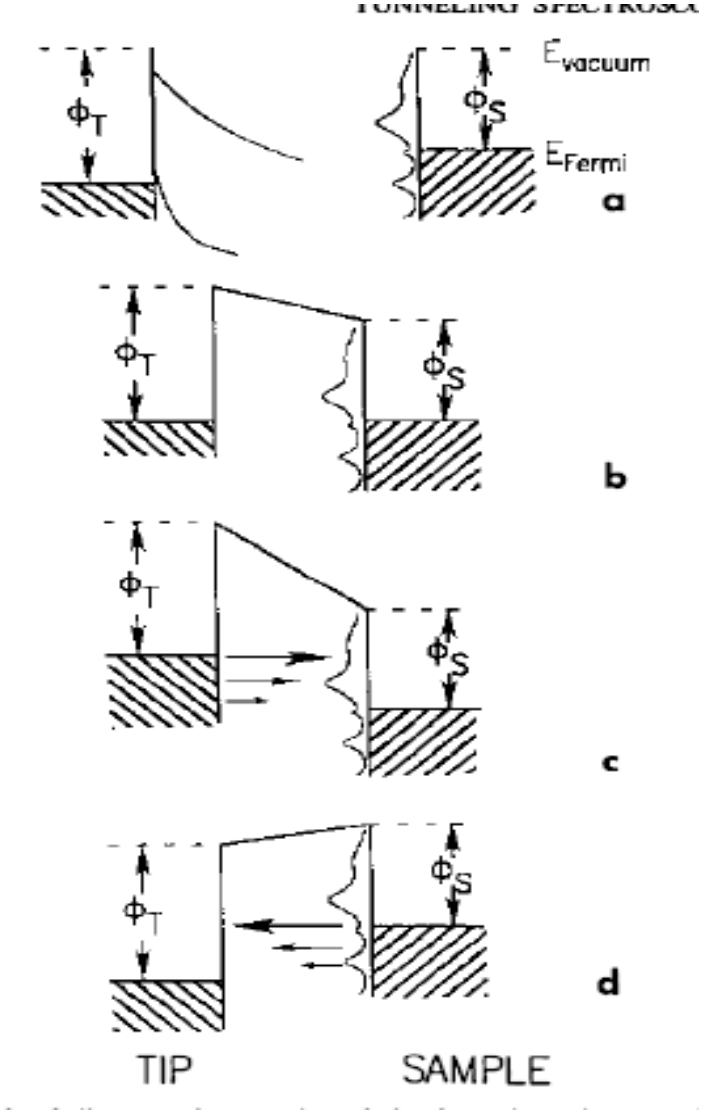

Figure 1.4 Energy diagram for the sample and the tip.

(a) Independent sample and tip. (b) Sample and tip at equilibrium, separated by small vacuum gap. (c) Positive sample bias: electrons tunnel from tip to sample. (d) Negative sample bias: electrons tunnel from sample into tip. [10, 11]

In practice, we can obtain STS by observing the variation of the tunneling current I as a function of the bias V, while the tip is held at a fixed height over the sample. It provides an I-V curve which can be numerically differentiated to a dI/dV curve. Or we can also directly obtained dI/dV by using a modulation technique with a lock-in amplifier.

1.2.2. The Theory of STS

Here we follow the analysis of Chen [2]. For simplicity, we only consider the condition when the bias is small. Therefore, the tunneling matrix element can be approximated by a constant. We further assume that the density of states of the tip is independent of energy. Therefore, in Eq. 1.11, we can take both the matrix element and the density of states of the tip out of the integral to obtain:

$$I = \frac{4\pi e}{\hbar} |M|^2 \rho_t \int_{-\infty}^{\infty} \rho_s(E)[f(E-eV) - f(E)]dE \quad (1.13)$$

If the temperature is not very high, the distribution function satisfies a step function, thus:

$$f(E-eV) - f(E) \approx \begin{cases} 1, & 0 < E < eV, \\ 0, & otherwise. \end{cases} \quad (1.14)$$

Combining Eq. 1.13 and Eq. 14, we can get:

$$I \propto \int_0^{eV} \rho_s(E)dE, \quad (1.15)$$

or,

$$\frac{dI}{dV} \propto \rho_s(E) \quad (1.16)$$

Thus, within those approximations, the differential conductance is directly proportional to the LDOS of the surface.

1.3. Atomic and Molecular Manipulation with the STM

Since the early 1990s, the application of STM has made possible manipulation of individual atoms and molecules on the surface. An early demonstration of these capabilities was provided by Eigler and Schwerzer[1] who constructed an IBM logo with individual Xe atoms on Ni(110). Using STM manipulation techniques, one can construct quantum structures on an atom-by-atom basis, synthesize single molecules on a one-molecule-at-a-time-basis, and access single atom/molecule properties, as reviewed in Hla and Bai [12, 16].

A variety of different atomic/molecular manipulation processes with STM have now been realized. We can divide the processes into two classes in terms of the location of the manipulated atoms/molecules: parallel processes and vertical processes[4]. In parallel processes, the motion of the adsorbed atoms/molecules is parallel to the surface, i.e., they remain on the surface. While in vertical processes, atoms/molecules can be

transferred from the tip to surface, or vice versa. Here I will only focus on the parallel processes.

The parallel processes can be further divided into three categories by the mechanisms of the motion: sliding processes, field-assisted diffusion, and inelastic-electron tunneling (IET) induced manipulation. The corresponding manipulation mechanisms are chemical forces, electric fields, and tunneling electrons, respectively.

1.3.1. Sliding Process

The STM tip always exerts a force on an adsorbate bound to the surface. By adjusting the position of the tip, we can tune the magnitude and direction of the force. Thus, there is a potential to manipulate the adsorbate by pulling it across the surface. This is called a sliding process[4, 17].

A typical sliding process involves three steps: (1) vertically approaching the tip toward the adsorbate until the tip-adsorbate is close enough, (2) sliding the tip across the surface with the same tip-adsorbate distance, dragging the adsorbate along, and (3) retracting the tip away from the surface, leaving the adsorbate on the surface. (See Figure 1.5) Since the first observed sliding process reported on Xenon/ Ni(110)[1], it has been extended to many other systems, e.g. Fe/Cu(111)[18], Co/Cu(111)[19], and Pb on Cu(111)[20].

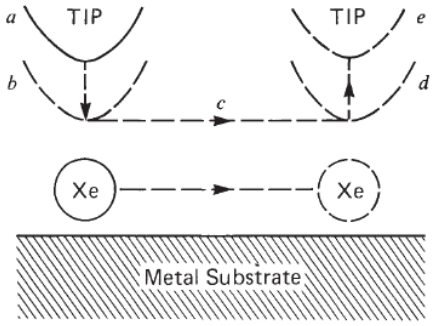

Figure 1.5 Schematic picture of the sliding process for a xenon atom[1].

(a) The adsorbate is located on the surface and the tip is placed directly over it. The tip is lowered to the position (b), where the adsorbate-tip attractive force is sufficient to keep the adsorbate located beneath the tip when the tip is subsequently moved across the surface (c) to the desired location (d). Finally the tip is withdrawn to position (e).

In most of those sliding process, the motion of the adsorbates is not sensitive to the sign or magnitude of the electric field, the voltage, or the current. It is only dependent on the tip-sample separation. In the case of a silver atom sliding on Ag(111)[21], the distance is 1.9Å between the edges of van der Waals radii of tip apex and the manipulated adsorbate. At this distance, the atomic orbitals of the tip apex and the adsorbate are overlapping and a weak chemical bond is formed, which is believed to be the mechanism of the atom/molecule motion in the sliding process.

Manipulation of single atoms/molecules on surfaces allows the construction of artificial quantum structures and the study of the novel phenomena associated with these structures. In addition, the possibility of constructing microscopic circuits has been

demonstrated. For example, Heinrich constructed a type of logic gate with CO/Cu(111)[19].

1.3.2. Field-Assisted Diffusion

There is a strong electric field between the tip and the surface in the normal STM scanning. This may induce field-assisted diffusion. Let us start by examining how close the tip is located near the sample in our case. In the previous section (Eq 1.8), we obtained a simple relation between conductance and the tip-sample distance: $G = \alpha G_0 e^{-2\kappa z}$ with $G_0 = \frac{2e^2}{h} \approx 77.48\mu S$, where α is a constant of order 1 in the limit of $\kappa Z \ll 1$[2]. z is the tip-sample distance where $z = 0$ is defined when the tip is in a single-atom contact with the sample. $\kappa = \frac{\sqrt{2m(U-E)}}{\hbar}$ is the decay constant. Take the vacuum level as the reference point of energy, $E = -\phi$, where ϕ is the work function. For simplicity, we take the average of the work functions of the tip and the sample, which is typical around 5eV. U is the applied bias and much smaller than the work functions. So

$$\kappa = 5.1\sqrt{\phi(eV)}nm^{-1} \approx 11.4nm^{-1}. \tag{1.17}$$

Under scanning conditions of $U = 1V$ and $I = 0.1nA$, $G = 0.1nS$. Then

$$z \approx 5.4\,\text{Å}. \tag{1.18}$$

The tip-sample distance z obtained by this simple analysis matches STM measurements [22-24].

If we use a rough estimation of $E = U / z$, the electric field is roughly on the order of 0.2 $V / \mathring{A}$. Under the real STM imaging conditions, due to the asymmetrical geometry, the electric field is inhomogeneous and concentrated in the vicinity of the tip. With a similar tip-sample distance and a bias of 1 to 10V, the electrical field strength is in the range from 0.2 to $2V / \mathring{A}$, as obtained by simulation[22]. Such large electrical fields approach those required for the ionization or desorption of an atom, which is around 3 to $5V / \mathring{A}$. The fields may also be large enough for field-assisted migration of adsorbates.

When an atom/molecule is adsorbed on the surface, it may have a static dipole or a dipole induced by the electric filed. As a first approximation,

$$\vec{p} = \vec{\mu} + \alpha \vec{E}, \tag{1.19}$$

where $\vec{\mu}$ is the permanent dipole moment, α is the polarizability of the adsorbate. As a result, the electric potential energy is given as

$$U(\vec{r}) = -\vec{\mu} \cdot \vec{E}(\vec{r}) - \frac{1}{2} \alpha \vec{E}(\vec{r})^2 . \tag{1.20}$$

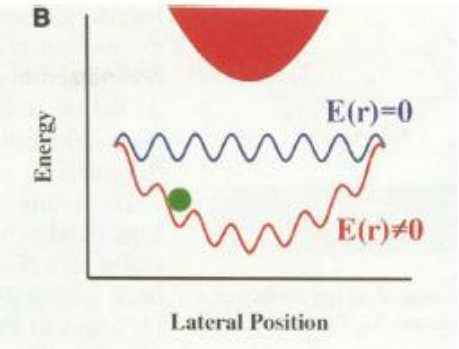

Figure 1.6 Schematic of the potential energy of an adsorbate on the surface as a function of the lateral position[4].

The tip is shown as the red solid object on the top. The interaction of the adsorbate and the surface atoms gives rise to a periodic potential energy (shown in blue). The interaction of the tip-induced electric field and the adsorbate gives rise to a broad potential well. Adding these two potentials together leads to a broad potential well located beneath the tip with periodic oscillations. The adsorbate is drawn as the green ball.

This potential energy is added to the periodic potential of the surface (Fig 1.6).

Note that there are two terms in the equation. If the second term dominates, then the adsorbate will always to be attracted to the tip. When the first term dominates, the orientation of the dipole moment remains unchanged, causing the direction of the adsorbate motion to reverse with the bias polarity, as shown in Figure 1.7.

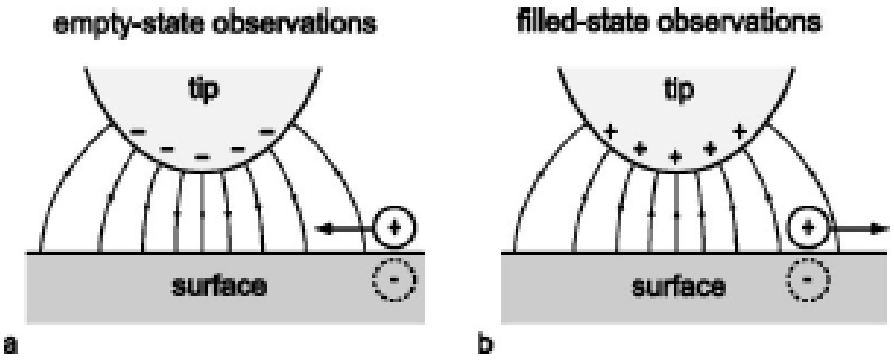

Figure 1.7 Schematic of the behavior of the polarized adsorbate in the nonuniform electric field induced by the STM tip[7].

The adsorbate has a downward dipole after charge transfer with the surface. (a) At a positive sample bias, the electric field direction is pointing from the surface to the tip with a parallel component pointing inward to the tip apex, causing the adsorbate to migrate inward.

A number of field-assisted diffusion experiments with STM have been reported. Depending on the relative magnitudes of the first (static dipole) and second (induced dipole) term in Eq 1.20, different types of behavior have been observed [4, 7, 16, 23-30]. When the induced dipole dominates, the adsorbate will be attracted to the tip irrespective of the polarity[29]. When the static dipole term dominates, such as thallium/Si(100) and In/Si(100)[7, 25], the adsorbates diffuse in opposite directions at different bias. For Cs atoms on GaAs and InSb(110) surfaces, the two terms are of comparable magnitude and the diffusion towards the tip only takes place at positive bias[26].

1.3.3. Inelastic-Tunneling-Induced Manipulation

Controlled excitations of atoms/molecules by using inelastic-electron tunneling induced manipulation processes have also been observed [3, 16, 31-40]. In this type of process, the tunneling electron energy is transferred to the adsorbate through a resonance state[37] no matter whether the current is tunneling from the tip to the surface or vice versa. The maximum available energy is determined by the bias, so atomic/molecular excitation usually exhibits a sudden onset at a threshold bias. The excitation rate can be varied by changing the current due to the change of the number of electrons tunneling.

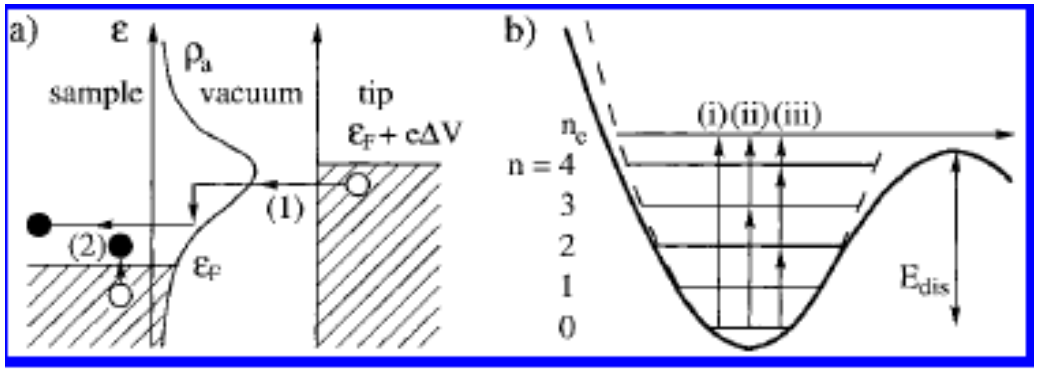

Figure 1.8 Schematic depicting the essential steps in the theoretically modeling of single O_2 molecule dissociation on Pt(111).[3]

(a) Vibrational relaxation occurs due to energy transfer from the tunneling electron. (b) The number of electrons needed to break the bond for different microscopic processes.

For molecular excitations, different excitation modes can be induced, such as rotational, vibrational, and electronic excitation. In addition, bonding breaking and bond formation

can also be realized. As shown in Fig 1.8, a tunneling electron inelastically scatters from an adsorbed molecule and transfers energy to the vibrational modes of the molecule. Then an energy barrier of bonding-breaking/formation needs to overcome via one or multiple vibrational excitations in the ground excitation states.

In some cases, the excitation modes will also decay into parallel motion. Take vibrational excitation as an example [39, 40]. When a tunneling electron is injected into the unoccupied states of an adsorbate, the molecule forms a temporary ionic state. When the electron then tunnels into the substrate, the molecule goes back to the neutral state. During the process, the nuclear positions of the molecule could be changed due to the Coulomb potential change, which leads to the excitation of vibrations. After this, the vibrational excited state can decay with two ways. One is to decay directly to an electron-hole pair, the other is to decay into a low-frequency translational mode, which is associated with the lateral motion of the molecules.

The injected the electrons can be tuned to selectively excite different modes of the adsorbate. For example, by selecting different pulse conditions for ammonia on Cu(100), Pascual et al.[34] could activate either the molecule stretching vibration or the inversion mode.

1.4. Experiment Setup

1.4.1. STM operations

The schematic of the basic STM operation is shown in Figure 1.9. The sample is grounded, a tunneling bias V_{gap} is applied to the tip, and a tunneling current is detected through a current amplifier. The control of the tip movement along x, y, and z-direction is realized by the piezos on which the tip is mounted. When a voltage is applied to a piezo, a mechanical deformation occurs, leading to the tip movement. This is called the inverse piezoelectric effect[2]. The piezoelectric strain coefficient can reach the order of 10^{-10}m/V, which enables precise control of the tip-sample distance in STM measurements.

The feedback circuit works differently in different modes: constant-height mode and constant-current mode. In both of the modes, the tip moves in the x and y direction by the control of the x, y-piezo. In the constant-height mode, the tip is kept at a fixed height, and the current is converted to voltage by the amplifier and recorded. In the constant-current scanning mode, the current is converted to voltage and then compared with the reference voltage. If the tunneling current is larger than the setpoint, then the voltage applied to the z-piezo will withdraw the tip from the surface, and vice versa. In this way, the tip can accurately follow the constant tunneling current contour at a high speed without the danger of crashing the tip. Therefore, it is more popular than the constant-height mode.

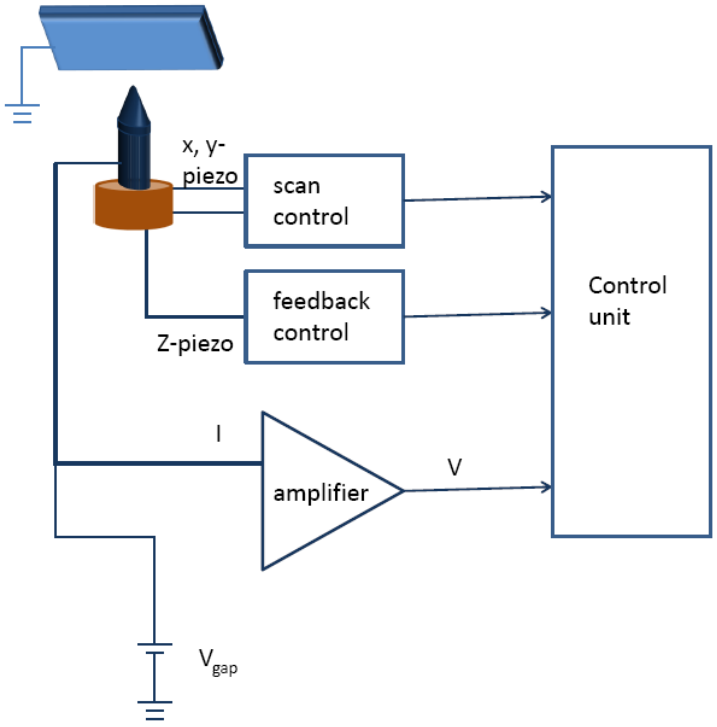

Figure 1.9: Schematics of STM operation.

Sample is grounded and the tip is biased. The tunneling current is detected with the amplification of an amplifier. The movement of the tip is controlled by the underneath piezos.

Another key issue in STM operations is vibration isolation. For metal surfaces, the atomic corrugation can be of the order of 0.01nm. Therefore, the tip-sample distance change caused by vibrations must be under picometer scale. In our STM, the vibration isolation is realized through three stages. The first stage is through a pneumatic system, isolating the whole chamber from the floor, which can isolate vibrations above its natural frequency of 1-2 Hz[2]. Secondly, the scanning stage of the STM is suspended

from the rest of chamber with springs, further isolating the scanning stage from the rest of the chamber above their natural frequency (typically 1-6 Hz[10]). Finally, the STM stage is also equipped with an eddy-current damper. When the metal pieces move relative to the magnetic field, damping forces are generated by eddy currents induced in the metal pieces, stabilizing the vibration of the system. Combining all three damping systems, the vibration is well controlled under picometer scale.

The STM used in our studies is an Omicron Low-temperature STM. It is capable of making measurements at a temperature as low as 5K. The entire chamber is divided into three smaller chambers by gate valves. Each chamber is pumped by ion pump or turbo pump/mechanical pump and can reach a pressure of 10^{-11} Torr.

In Figure 1.10a, the left tall chamber is the STM chamber with two cryostats and a sample-stage couter-heater. If the scanning temperature is around 77K, then both of the cryostats are filled with liquid nitrogen; if the scanning temperature is around 5K, then the inner cryostat is filled with liquid helium and the outer one with liquid nitrogen. For any other specific temperature, pumping or counter-heating is necessary.

The right smaller chamber in Figure 1.10a is the preparation chamber, which is equipped with LEED (low energy electron diffraction), Auger spectrometer, heaters, sputtering gun, mass spectrometer and a few leak valves that can allow gas dosage into the chamber. LEED detects the structure of the top few layers of the sample surface.

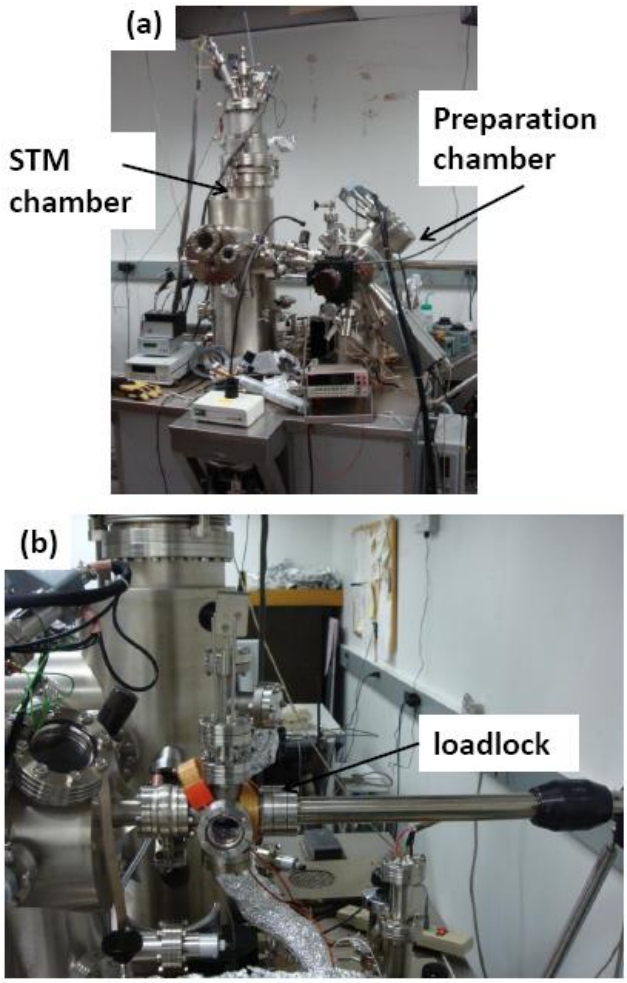

Figure 1.10: A front view and a side view of Omicron LTSTM.

(a) A front view picture and (b) a side view picture of Omicron LTSTM. The chambers are labeled in the picture.

Auger spectrometer measures the chemical components and their portions of the surface. Mass spectrometer analyzes the mass/charge ratio of the gas in the chamber. In our experiments, we perform the surface preparation and characterizations in this chamber. For example, the precut Au(111) is sputtered and annealed, and then it is characterized

by LEED and Auger spectrometer in this chamber. We then transfer the sample to the STM chamber after a clean surface and an ordered structure is obtained. We can also introduce gases into this chamber via leak valves and deposit them onto the samples in this chamber.

On the side of the preparation chamber, there is a loadlock (shown in Figure 1.10b). As the name implies, the samples are loaded through it from ambient to the preparation chamber. Sometimes, we also dose large molecules with higher evaporation temperature in this chamber.

1.4.2. Molecule Dosing

There is an important unit used in dosing molecule: Langmuir, which is described by multiplying the pressure of the dosing gas and the dosing time. One Langmuir corresponds to an exposure of one second to a gas with a pressure of 10^{-6} Torr[41, 42]. For example, if the dosing pressure is 10^{-8} Torr and the dosing time is 100 seconds, we get one Langmuir dosage. From kinetic theory[43], the rate of the gas molecule impinging on the surface is given by:

$$\frac{dN}{dt} = \frac{P}{\sqrt{2\pi MkT}} = \frac{3.51\times10^{22} P(Torr)}{\sqrt{MT}} cm^{-2}s^{-1}, \qquad (1.21)$$

where M is the gas molecule mass in a.m.u., T is the temperature in Kevin, and P is the pressure in Torr. As an example, if we dose CO molecules of M=28, at a pressure of

10^{-6} Torr and a temperature of 300K, $\frac{dN}{dt} = 3.8 \times 10^{14} cm^{-2} s^{-1}$. If every impinging gas molecule sticks to the surface, then within one second, the total number of the gas molecules on the surface is $N = 3.8 \times 10^{14} cm^{-2}$, which is comparable to the surface atom density, $\sim (10^{23} cm^{-3})^{\frac{2}{3}} \sim 10^{15} cm^{-2}$. Therefore, one Langmuir corresponds to roughly one monolayer of coverage. In practice, the sticking coefficient might be lower than the ideal situation which makes a precise estimation difficult.

In our experiments, there are two ways to dose molecules. For the 1,4-benzenediamine (BDA) case, we dosed the molecules through a leak valve to the preparation chamber where the sample is sitting. As shown in Figure 1.11, BDA is bottled in a glass cylinder outside of the preparation chamber. One side of it is pumped by turbo pump/mechanical pump; the other side is connected to the preparation chamber via a leak valve. In order to increase the vapor pressure, the sample is heated to 100^{o}C while dosing. For the contorted hexabenzocoronene (HBC) case, the sample is brought to the loadlock where the molecule is thermally heated to 605K.

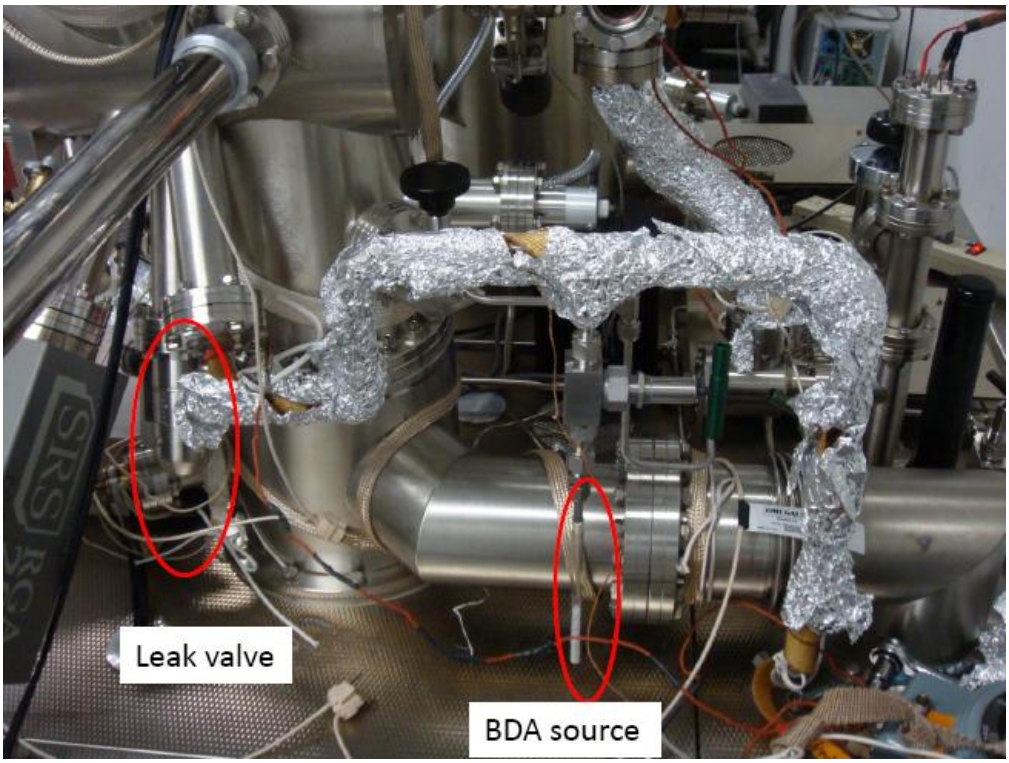

Figure 1.11: Picture of 1,4-benznediamine (BDA) dosing line.

The BDA molecules are bottled in a glass cylinder in a red circle and connected to pumps on one side and the preparation chamber via a leak valve (in a red circle) on the other side.

1.4.3. Tip preparation

As mentioned above, the atomically sharp tip is very important to the imaging quality. In our study, we used the electro-mechanical etching method, which is by now a standard method in tip preparation[2] .

In this method, the tungsten wire is connected to the anode, and a metal cylinder is immersed in the solution as a cathode (see Figure 1.12a). The wire is lowered into the

solution until a meniscus is formed (Figure 1.12b). The meniscus is a key factor to determine the shape and length of the tip end. The etching speed at the top of the meniscus is lower than that of the bottom due to a concentration gradient of OH^- ions[5]. As a result, a neck is formed on the wire at the interface of air and the solution and it becomes thinner and thinner. Eventually the wire will break due to the gravity of the lower part of the wire. In this way, two tips from the top portion and the bottom portion are made simultaneous. The overall electrochemical reaction[2] is:

Cathode: $6H_2O + 6e^- \rightarrow 3H_2(\uparrow) + 6OH^-$

Anode: $W + 8OH^- \rightarrow WO_4^{2-} + 4H_2O + 6e^-$

Total: $W + 2OH^- + 2H_2O \rightarrow WO_4^{2-} + 3H_2(\uparrow)$

In our experiment, we replace the metal cylinder by a platinum wire (see Figure 1.12c) and use a thin membrane of the solution to etch the tip. We found it work best with a DC current of 3-5V, a polycrystalline tungsten wire of 2.5mm diameter, and a 3 mol/L NaOH solution. As mentioned above, we could make two tips at one time. The bottom tip is usually sharper and longer than the top one, and therefore can reach atomic resolution more easily. This can be explained by the difference of the current cut-off time[5]. As the bottom tip drops due to gravity, it stops being etched immediately whereas the top tip is still being etched until the current is manually shut off.

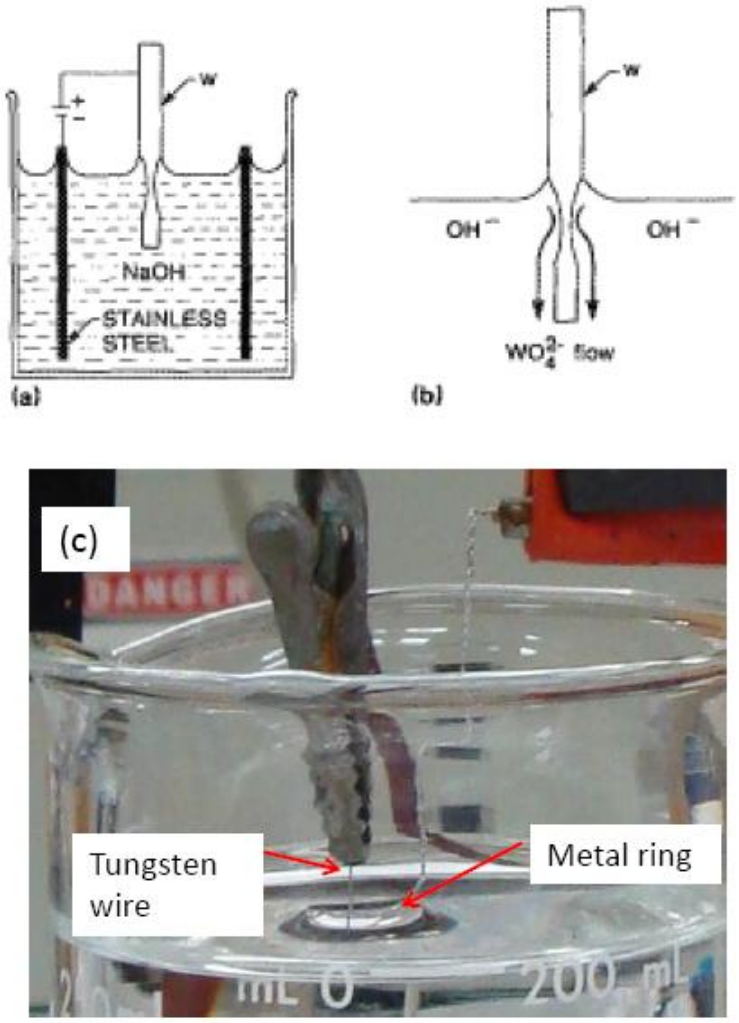

Figure 1.12: Electrochemical etching of tungsten tips.

(a) A schematic of an instrument setup of tip making[5]. (b) A schematic of the etching process, showing a meniscus formed on the wire while etching. (c) The picture of our setup with a metal ring as a cathode.

After etching, the tip is transferred to the vacuum chamber. However, electrochemical etching cannot guarantee atomic sharpness. In fact, the typical tip diameter is between 4-15nm after etching [44, 45]. There are many ways to further sharpen or reshape a blunt tip. In our study, we mainly used three methods: tip crashing, field emission, and annealing.

The tip crashing method refers literally to crashing the tip to the surface, mostly soft metals, in the hope of pulling surface atoms to the tip end and forming an atomically-sharp tip when the tip is retracted. Field emission is accomplished by applying high voltage (~10V) and high current (5-10nA) when the tip is in the tunneling regime with the surface. This phenomenon can be explained with the restructuring of the tungsten atoms in the tip under a high electric field[2]. Tip annealing is used to remove the tungsten oxide and other impurities from the tip. In practice, we combine all three methods in the hope of getting a perfect tip.

1.5. Bibliography

1. Eigler, D.M. and E.K. Schweizer, *Positioning single atoms with a scanning tunneling microscope.* Nature, 1990. **344**(6266): p. 524-526.

2. Chen, C.J., *Introduction to Scanning Tunneling Microscopy*. 2 ed. Vol. 1. 2008: Oxford University Press.

3. Ho, W., *Inducing and Viewing Bond Selected Chemistry with Tunneling Electrons.* Accounts of Chemical Research, 1998. **31**(9): p. 567-573.

4. Stroscio, J.A. and D.M. Eigler, *Atomic and Molecular Manipulation with the Scanning Tunneling Microscope.* Science, 1991. **254**(5036): p. 1319-1326.

5. Ibe, J.P., et al., *On the electrochemical etching of tips for scanning tunneling microscopy.* Journal of Vacuum Science & Technology A: Vacuum, Surfaces, and Films, 1990. **8**(4): p. 3570-3575.

6. Binnig, G. and H. Rohrer, *Scanning tunneling microscopy.* IBM J. Res. Dev., 1986. **30**(4): p. 355-369.

7. Saranin, A.A., et al., *Growth of thallium overlayers on a Si(100) surface.* Physical Review B, 2005. **71**(3): p. 035312.

8. Tersoff, J. and D.R. Hamann, *Theory and Application for the Scanning Tunneling Microscope.* Physical Review Letters, 1983. **50**(25): p. 1998.

9. Tersoff, J. and D.R. Hamann, *Theory of the scanning tunneling microscope.* Physical Review B, 1985. **31**(2): p. 805.

10. Wiesendanger, R., *Scanning Probe Microscopy and Spectroscopy: Methods and Applications*. 1994: Cambridge.

11. Hamers, R.J., *Atomic-resolution surface spectroscopy with the scanning tunneling microscopy.* Annual Review of Physical Chemistry, 1989. **40**: p. 531-559.

12. Bai, C., *Scanning Tunneling Microscopy and its application*. Springer Series in Surface Sciences, ed. R.G. Gerhard Ertl, Douglas L. Mills, Ing. Helmut K. V. Lotsch. Vol. 32. 1995, Shanghai: Springer.

13. Laudauer, R., *many-channel conductance formula.* IBM J. Res. Dev., 1957. **21**.

14. Bardeen, J., *Tunnelling from a Many-Particle Point of View*. Physical Review Letters, 1961. **6**(2): p. 57.

15. Lang, N.D., *Apparent Size of an Atom in the Scanning Tunneling Microscope as a Function of Bias.* Physical Review Letters, 1987. **58**(1): p. 45.

16. Hla, S.W., *Scanning tunneling microscopy single atom/molecule manipulation and its application to nanoscience and technology.* Journal of Vacuum Science & Technology B, 2005. **23**(4): p. 1351-1360.

17. Eigler, D.M., C.P. Lutz, and W.E. Rudge, *An atomic switch realized with the scanning tunnelling microscope.* Nature, 1991. **352**(6336): p. 600-603.

18. Crommie, M.F., C.P. Lutz, and D.M. Eigler, *Confinement of Electrons to Quantum Corrals on a Metal Surface.* Science, 1993. **262**(5131): p. 218-220.

19. Heinrich, A.J., et al., *Molecule cascades.* Science, 2002. **298**(5597): p. 1381-1387.

20. Bartels, L., G. Meyer, and K.H. Rieder, *Basic Steps of Lateral Manipulation of Single Atoms and Diatomic Clusters with a Scanning Tunneling Microscope Tip.* Physical Review Letters, 1997. **79**(4): p. 697.

21. Hla, S.W., K.F. Braun, and K.H. Rieder, *Single-atom manipulation mechanisms during a quantum corral construction.* Physical Review B, 2003. **67**(20): p. 4.

22. Yazdani, A., D.M. Eigler, and N.D. Lang, *Off-Resonance Conduction Through Atomic Wires.* Science, 1996. **272**(5270): p. 1921-1924.

23. Akiyama, R., T. Matsumoto, and T. Kawai, *A Scanning Tunneling Microscopy Study of Electrostatic and Proximity Effects in Tip-Assisted Migration and Desorption of a DNA Base Molecule on SrTiO3.* The Journal of Physical Chemistry B, 1999. **103**(29): p. 6103-6110.

24. Akiyama, R., T. Matsumoto, and T. Kawai, *Mechanism of tip-assisted migration and desorption of DNA base molecules on an $SrTiO_3$ surface.* Applied Physics A: Materials Science & Processing, 1998. **66**(0): p. S719-S722.

25.Saranin, A.A., et al., *STM tip-induced diffusion of In atoms on the Si(111) $\sqrt{3} \times \sqrt{3}$- In surface.* Physical Review B, 1997. **56**(12): p. 7449.

26. Whitman, L.J., et al., *Manipulation of Adsorbed Atoms and Creation of New Structures on Room-Temperature Surfaces with a Scanning Tunneling Microscope.* Science, 1991. **251**(4998): p. 1206-1210.

27. Kim, J., et al., *Local atomic diffusion on Au(III) surface induced by Au tip.* Japanese Journal of Applied Physics Part 1-Regular Papers Short Notes & Review Papers, 2003. **42**(6A): p. 3616-3618.

28. Nakayama, T., D.H. Huang, and M. Aono, *Extraction, deposition, and displacement of atoms by STM.* Microelectronic Engineering, 1996. **32**(1-4): p. 191-201.

29. Tsong, T.T., *Effects of an electric field in atomic manipulations.* Physical Review B, 1991. **44**(24): p. 13703.

30. Tsong, T.T. and C.-S. Chang, *High Field Effects and Methods Useful for Transferring Atoms in Scanning Tunneling Microscope.* Japanese Journal of Applied Physics, 1995. **34**(Part 1, No. 6B): p. 3309.

31. Stipe, B.C., M.A. Rezaei, and W. Ho, *Inducing and Viewing the Rotational Motion of a Single Molecule.* Science, 1998. **279**(5358): p. 1907-1909.

32. Stipe, B.C., M.A. Rezaei, and W. Ho, *Coupling of Vibrational Excitation to the Rotational Motion of a Single Adsorbed Molecule.* Physical Review Letters, 1998. **81**(6): p. 1263.

33. Stipe, B.C., M.A. Rezaei, and W. Ho, *Single-Molecule Vibrational Spectroscopy and Microscopy.* Science, 1998. **280**(5370): p. 1732-1735.

34. Pascual, J.I., et al., *Selectivity in vibrationally mediated single-molecule chemistry.* Nature, 2003. **423**(6939): p. 525-528.

35. Bartels, L., et al., *Atomic-scale chemistry: Desorption of ammonia from Cu(111) induced by tunneling electrons.* Chemical Physics Letters, 1999. **313**(3-4): p. 544-552.

36. Bilic, A., et al., *Adsorption of ammonia on the gold(111) surface.* Journal of Chemical Physics, 2002. **116**(20): p. 8981-8987.

37. Gadzuk, J.W., *Resonance-assisted, hot-electron-induced desorption.* Surface Science, 1995. **342**(1-3): p. 345-358.

38. Gaudioso, J., H.J. Lee, and W. Ho, *Vibrational Analysis of Single Molecule Chemistry:鈥?Ethylene Dehydrogenation on Ni(110).* Journal of the American Chemical Society, 1999. **121**(37): p. 8479-8485.

39. Komeda, T., et al., *Lateral Hopping of Molecules Induced by Excitation of Internal Vibration Mode.* Science, 2002. **295**(5562): p. 2055-2058.

40. Persson, B.N.J. and H. Ueba, *Theory of inelastic tunneling induced motion of adsorbates on metal surfaces.* Surface Science, 2002. **502-503**: p. 18-25.

41. *International Union of Pure and Applied Chemistry*. 1993.

42. *Quantities, Units and Symbols in Physical Chemistry*. 2nd ed: Oxford: Blackwell Science.

43. Salzman, W.R., *Lecture notes*, University of Arizona.

44. Muller, A.D., et al., *Characterization of electrochemically etched tungsten tips for scanning tunneling microscopy.* Review of Scientific Instruments, 1999. **70**(10): p. 3970-3972.

45. Kazinczi, R., et al., *Novel methods for preparing EC STM tips.* Applied Physics a-Materials Science & Processing, 1998. **66**: p. S535-S538.

Chapter 2

Au(111) Substrate and Preparation

Gold is one of the most popular substrates for molecular analysis in STM studies because it is chemically inert, conductive, and easily prepared. Gold is a soft material, therefore we can also use it in the tip-crash method to restore the STM tip.

Among all the facets, Au(111) is the most stable and can be most easily prepared. Therefore, it is widely used in STM studies. It can usually be obtained by sputtering and annealing from pre-cut Au(111) single crystals or flame annealing from thin gold films on mica (discussed in more detail in Section 2.2).

2.1. Introduction to Gold and Au(111) Surface

The crystal structure of bulk gold is a face-centered cubic (fcc) lattice with a lattice constant of 4.08Å[1]. The (111) plane is defined by the atoms at [100], [010], and [001], resulting in a hexagonal lattice plane (See Figure 2.1).

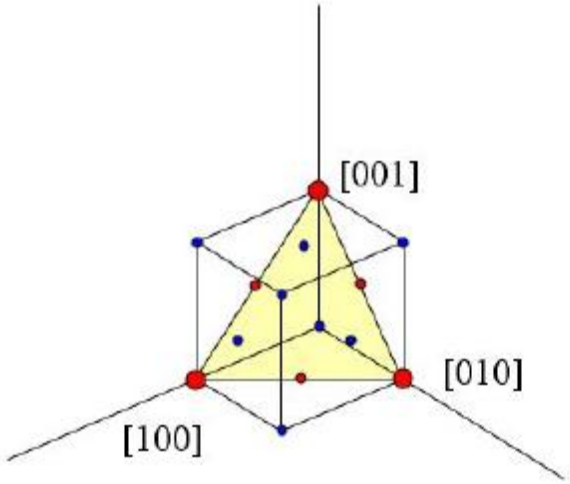

2.1: Schematic of the crystal structure of bulk gold and the surface of (111).

The blue and red dots indicate the gold atom positions inside of the bulk crystal. The Au(111) is defined by 3 big red gold atoms and has 3 additional red atoms from the cube. Au(111) has a hexagonal lattice structure.

The Au(111) surface, however, can exhibit either fcc structure or hexagonal closed-packed (hcp) structure depending on how the gold top layer atoms are stacked. In Figure 2.2, the different structures of fcc and hcp structures are illustrated. In the fcc structure, the Au atoms occupy three different locations at three layers (ABC stacking). Whereas

in the hcp structure, the top layer Au atoms overlap with the bottom layer atoms (ABA stacking). From a first-principle calculation by Takeuchi et al.[2], the energy of the fcc structure is the lowest. The hcp structure and bridge sites have slightly bigger energy with only 1mRy and 3mRy bigger than fcc structure, respectively. The top site has the highest energy which is 14mRy larger than fcc site. Since the energy of the fcc and hcp structure is very close, it is possible to have both structures coexisting on the surface.

Both of the fcc and hcp structures can coexist on Au(111) surface. When the two different structures meet, there is a buckling from the rest areas of the surface, resulting in the famous "herringbone" reconstruction ridges [3-9]. This reconstruction has about 4.4% contraction along $[1\bar{1}0]$, placing 23 Au atoms onto 22 atom locations. Therefore, the unit cell of this reconstruction is $(22\pm1)\times\sqrt{3}$. The ridges are higher than the rest of the surface by ~ 0.2Å (Figure 2.3).

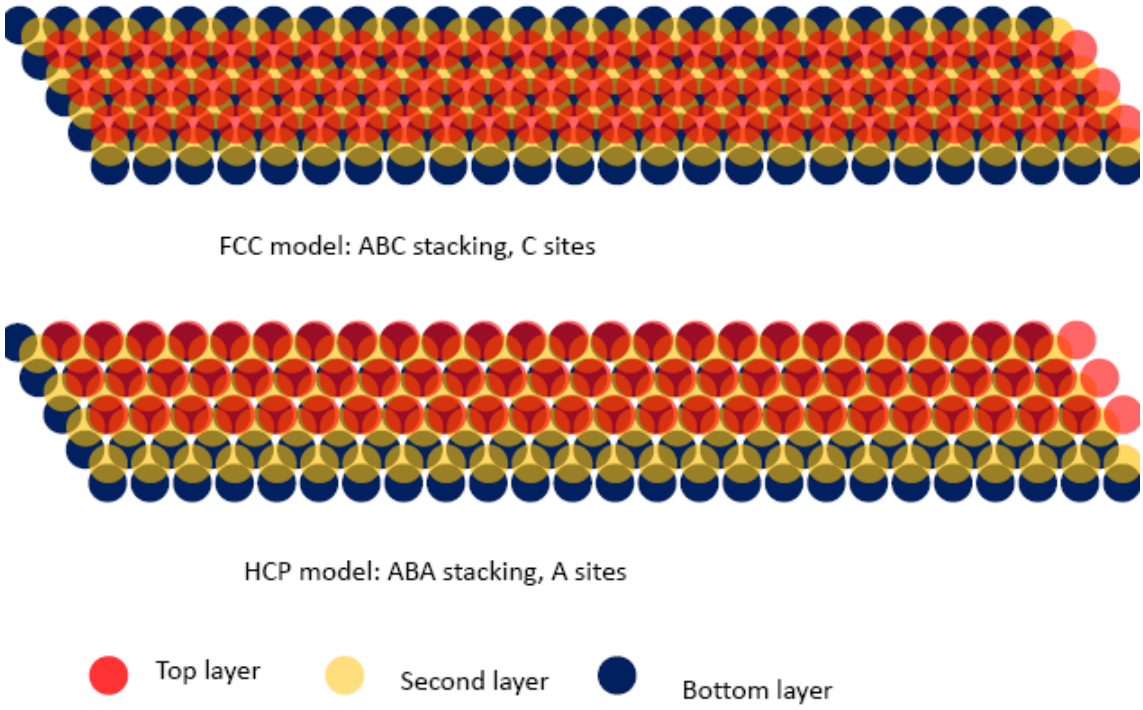

Figure 2.2: Schematic of the top three layers of the fcc and hcp structures.

The upper panel is the fcc structure, where the Au atoms occupy three different locations at three different layers (ABC stacking). The lower panel is the hcp structure, where the top layer Au atoms overlap with the bottom layer atoms (ABA stacking). The red, yellow, and blue dots indicate the Au atoms located on the top, second, and bottom layers, respectively. (Courtesy of Kwang Taeg Rim)

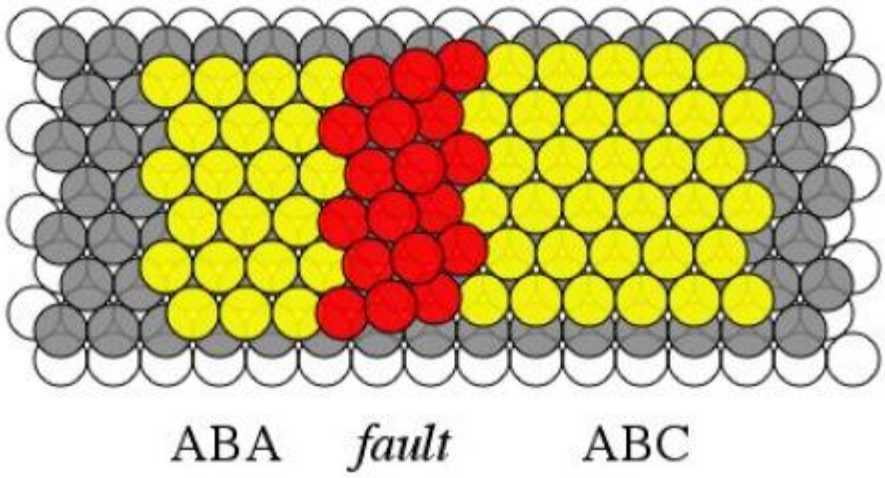

Figure 2.3: Hard sphere model of one stacking fault region in Au(111).

The atoms (yellow) have ABA stacking (hcp structure) on the left, and ABC stacking (fcc structure) on the right, respectively. When they meet in the middle (red), they are forced to occupy bridge sites of the second layer and therefore buckle from the surface.

This herringbone structure is visible in STM measurements of the clean Au(111) surface (Figure 2.4). The fcc region (38Å) are a little wider than the hcp region (25Å) [10]. This feature makes it easy to distinguish the two different regions. The reconstruction is very sensitive to the impurities on the surface; therefore, it is, in practice, an indication of the cleanness of the surface[11, 12]. Sometimes, the Au(111) surface has other reconstructions due to a small amount of local defects, such as step edges or impurities. For example, we observed U-shaped reconstruction patterns near the steps in Figure 2.5(a), which is also reported by Barth et al.[3]. We also observed a triangular reconstruction pattern which is shown in Figure 2.6.

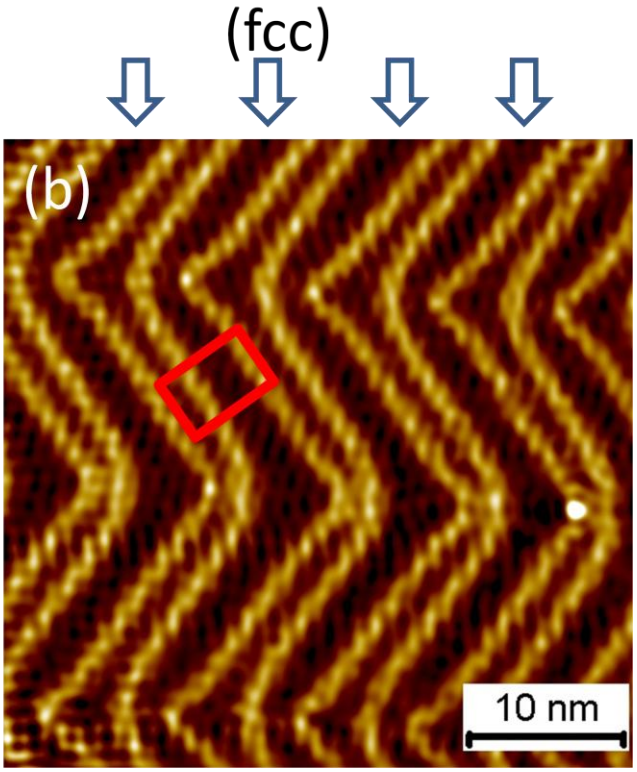

Figure 2.4: STM topography of Au(111) surface.

A typical flat and clean Au(111) surface is shown with the red box indicating the area of the hard sphere models in Figure 2.3. The scanning condition is 1V, 0.5nA. Blue arrows indicate the positions of fcc structures.

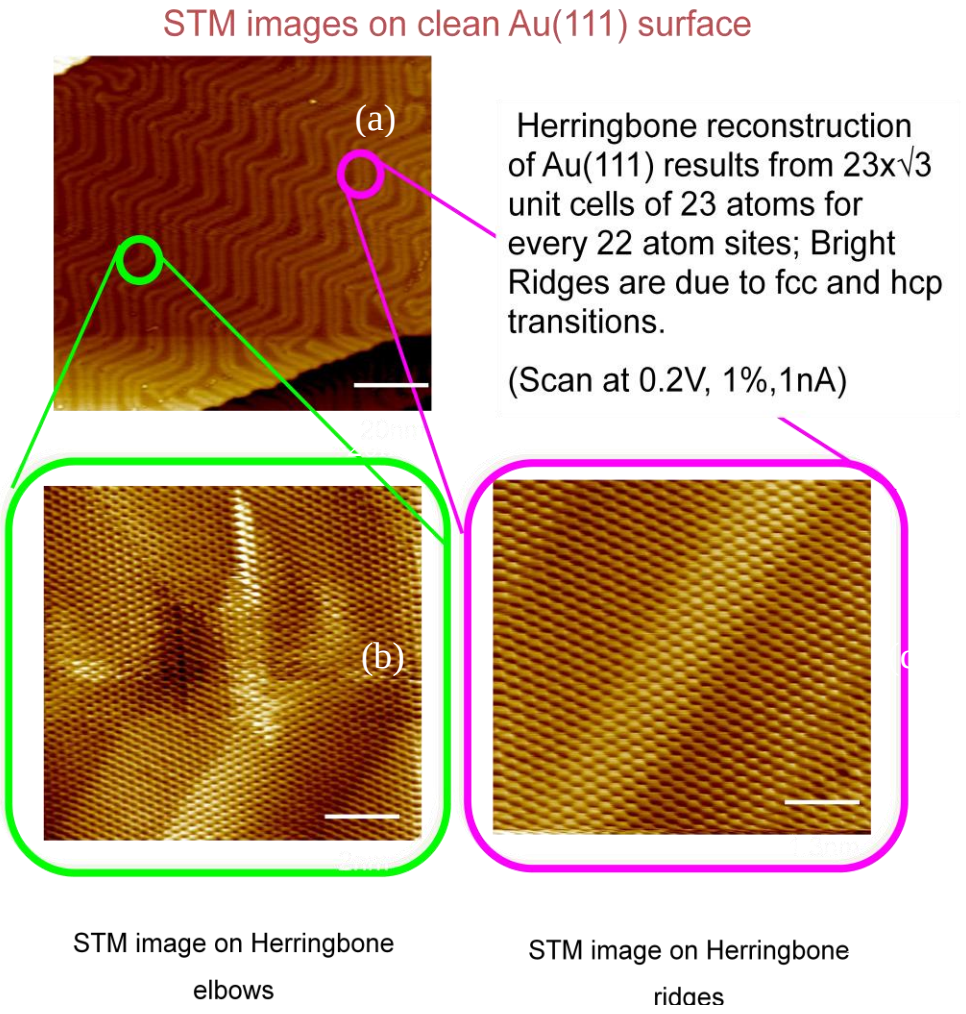

Figure 2.5: Atomic resolution STM topography of Au(111) herringbone elbow sites and ridge sites.

(a) A large, clean Au(111) terrace with ~100nm width is shown. Near the two steps in this region, the herringbone reconstruction turns irregular. Green and pink circles illustrate the location of one herringbone elbow and one ridge site. (b) Atomic resolution image of a herringbone elbow site zoomed in from green circle in (a) shows a distortion of atom arrays at the elbow. (c) Atomic resolution image of a herringbone ridge zoomed in from pink circle in (a) shows a regular array of Au atoms. The scanning condition is 0.2V, 1nA.

Shown in Figure 2.5(b-c) is the atomic resolution STM image of the herringbone structure, Figure 2.5(b) clearly indicates a distortion of atom positions and brightness at an elbow site, due to either the local electronic or atomic structure. Figure 2.5(c) shows a regular array of atoms on a ridge.

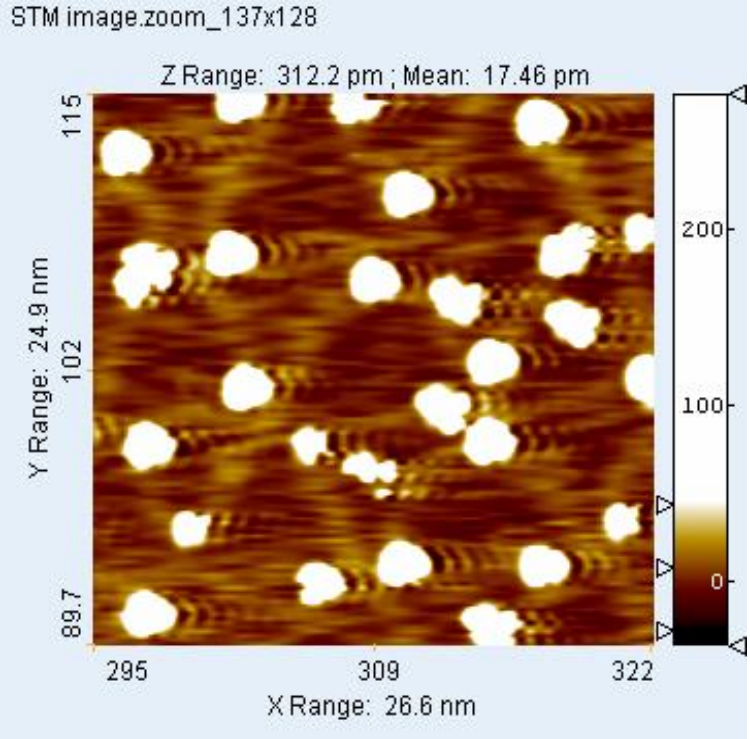

Figure 2.6: Triangle reconstruction STM topography of Au(111).

The underlying surface is shown with triangle reconstruction. The bright dots are evaporated molecules. The scanning size is 26.6x24.9nm^2. The waves near the bright dots are standing waves reflected from the defects.

At different parts of the herringbone reconstruction, the reactivity is possibly different. The herringbone elbow sites are reported to be one of the most reactive sites on this

surface. STM studies on preferential nucleation of Ni, Fe and Co[8, 13, 14] on these sites have suggested that these sites might be energetically favored to capture atoms that are diffusing on the surface.

The difference in the reactivity of fcc, hcp and ridge sites of the Au(111) herringbone has also been reported. For example, STM studies on thiolates on Au(111)[15, 16] show preferential adsorption of the molecule on the fcc sites. A DFT calculation[17] found out that Au-Au distances around the fcc sites elongate by a large distance upon thiolate adsorption and the relaxation propagates to the second layer, while there are weaker effects in the hcp configuration. As a result, the binding energy of thiolates on fcc sites is about 0.24eV larger than hcp sites.

2.2. Au(111) Preparation

As previously mentioned, there are usually two methods to obtain Au(111) surface. One way is to obtain it from a thin gold film evaporated on other substrates, such as mica. Since (111) is the most stable facet for Au, Au(111) is usually obtained from evaporation. Average roughness of the as-evaporated thin film is on the nanometer scale. Then one uses flame-annealing technique to remove the contaminants and flatten the surface. In this procedure, the typical gas used is hydrogen or butane. In the case of hydrogen, the Au-mica substrate is quickly passed through a 1100^{o}C flame, 1-2cm above the blue portion of the flame[18]. This method is fast, but requires some experience. Furthermore, it is done ex-situ and we still need at least a few minutes to

transfer the sample into the vacuum chamber which may involve some additional contaminants.

In our study, we adopted an alternative way, obtaining it in-situ from a pre-cut single crystal. In this way, we use repeated cycles of sputtering to remove the surface contaminants and subsequent annealing to flatten the surface and bring the contaminants from the bulk to the surface. In the sputtering procedure, the UHV chamber is backfilled with $1x10^{-5}$ Torr argon gas and a 0.5keV ion beam is focused onto the sample with about 3μA sample current. In the annealing procedure, we use indirect heating method by providing the heater with a 1.6A current, which is equivalent to about 600^{o}C. Each cycle includes a 15 min sputtering and a 15 min annealing. The cycle number varies from 3-20 cycles depending on the previous condition of the sample. It has been suggested that a prolonged cooling-down procedure might be the best for the smoothness of the sample. In our case, cooling down quickly does not affect the quality of the surface.

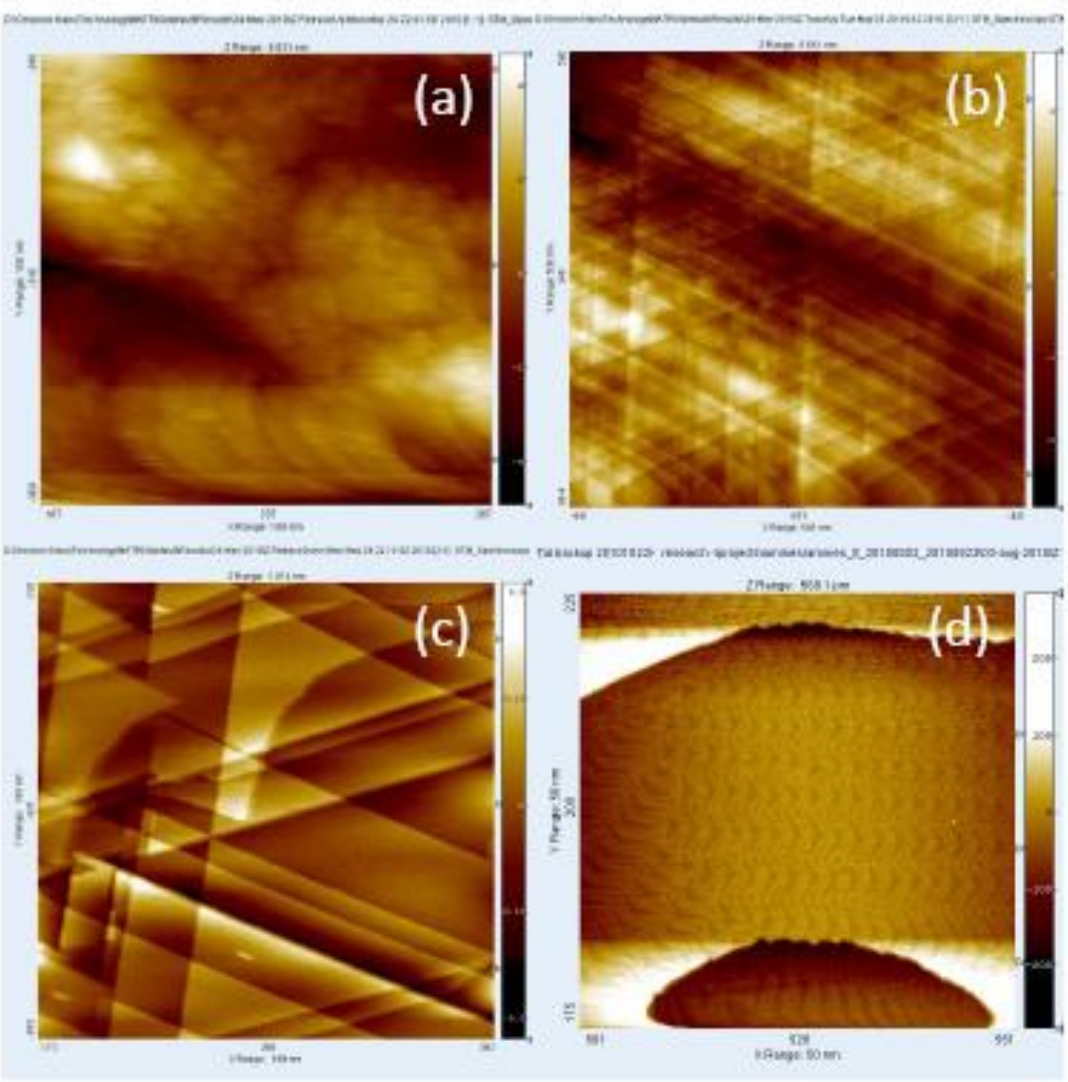

Figure 2.7: Large-scale STM topography of Au surface transition through sputtering and annealing

These images show the STM topography of the Au(111) surface (a) before, (b-c) during, and (d)after sputtering and annealing. The sizes of the images are (a) 100nmx100nm, (b) 500x500nm, (c) 189nmx189nm, and (d) 200x200nm.

Figure 2.7 shows the STM images before/during/after sputtering and annealing. Figure 2.7(a) shows the surface before the procedure, in which the surface is very rough with corrugation~10nm. After a few cycles, the top layer contaminants started to be removed and the gold surface starts to relax into ordered structures. In Figure 2.7(b), the surface starts to form narrow steps and triangular adlayers due to the influence of six-fold symmetry of Au lattice. However, the energy has not completely relaxed, so the herringbone reconstruction is not yet formed. In addition, there is still a small amount of impurities on the surface. In Figure 2.7(c), with more impurities removed, the surface started to have more ordered structure with large terrace ~30nm and herringbone reconstruction is very easily observed on the large terraces. In addition, there is a much less amount of impurities on the surface. With further sputtering/annealing, after most of the contaminants are removed, large terraces with ~200nm and the periodic herringbone reconstruction have formed as shown in Figure 2.7(d).

2.3. Bibliography

1. Kittel, C., *Introduction to Solid State Physics*. 7 ed. 1996: John Wiley and Sons.

2. Takeuchi, N., C.T. Chan, and K.M. Ho, *Au(111): A theoretical study of the surface reconstruction and the surface electronic structure.* Physical Review B, 1991. **43**(17): p. 13899.

3. Barth, J.V., et al., *Scanning tunneling microscopy observations on the reconstructed Au(111) surface: Atomic structure, long-range superstructure, rotational domains, and surface defects.* Physical Review B, 1990. **42**(15): p. 9307.

4. Davis, L.C., et al., *Theory of the local density of surface states on a metal: Comparison with scanning tunneling spectroscopy of a Au(111) surface.* Physical Review B, 1991. **43**(5): p. 3821.

5. El-Batanouny, M., et al., *Double-sine-Gordon solitons: A model for misfit dislocations on the Au(111) reconstructed surface.* Physical Review Letters, 1987. **58**(26): p. 2762.

6. Hallmark, V.M., et al., *Observation of Atomic Corrugation on Au(111) by Scanning Tunneling Microscopy.* Physical Review Letters, 1987. **59**(25): p. 2879.

7. Harten, U., et al., *Observation of a Soliton Reconstruction of Au(111) by High-Resolution Helium-Atom Diffraction.* Physical Review Letters, 1985. **54**(24): p. 2619.

8. Meyer, J.A., et al., *Preferential island nucleation at the elbows of the Au(111) herringbone reconstruction through place exchange.* Surface Science, 1996. **365**(1): p. L647-L651.

9. Wöll, C., et al., *Determination of atom positions at stacking-fault dislocations on Au(111) by scanning tunneling microscopy.* Physical Review B, 1989. **39**(11): p. 7988.

10. Chen, W., et al., *Scanning Tunneling Microscopy Observation of an Electronic Superlattice at the Surface of Clean Gold.* Physical Review Letters, 1998. **80**(7): p. 1469.

11. Rousset, S. and et al., *Self-ordering of Au(111) vicinal surfaces and application to nanostructure organized growth.* Journal of Physics: Condensed Matter, 2003. **15**(47): p. S3363.

12. Hasegawa, Y. and P. Avouris, *Manipulation of the Reconstruction of the Au(111) Surface with the STM.* Science, 1992. **258**(5089): p. 1763-1765.

13. Chambliss, D.D., R.J. Wilson, and S. Chiang, *Nucleation of ordered Ni island arrays on Au(111) by surface-lattice dislocations.* Physical Review Letters, 1991. **66**(13): p. 1721.

14. Tölkes, C., et al., *Preparation of well-ordered cobalt nanostructures on Au(111).* Physical Review B, 1997. **55**(20): p. 13932.

15. Fitts, W.P., J.M. White, and G.E. Poirier, *Low-Coverage Decanethiolate Structure on Au(111): Substrate Effects.* Langmuir, 2002. **18**(5): p. 1561-1566.

16. Maksymovych, P. and J.T. Yates, *Au Adatoms in Self-Assembly of Benzenethiol on the Au(111) Surface.* Journal of the American Chemical Society, 2008. **130**(24): p. 7518-7519.

17. Grönbeck, H., A. Curioni, and W. Andreoni, *Thiols and Disulfides on the Au(111) Surface: The Headgroup - gold Interaction.* Journal of the American Chemical Society, 2000. **122**(16): p. 3839-3842.

18. Mark, H.D., et al., *Preparation of gold thin films by epitaxial growth on mica and the effect of flame annealing.* Journal of Vacuum Science & Technology A: Vacuum, Surfaces, and Films, 1998. **16**(6): p. 3295-3300.

Chapter 3

Study of 1,4-benzenediamine Adsorption on Au(111)

3.1. Abstract

In this chapter, we apply STM to investigate the binding of a model amine compound, 1,4-benzenediamine (BDA), to the reconstructed Au(111) surface. We find that BDA exhibits different structures at different coverages, including isolated BDA at a low coverage, branched chain structures and network structure at an intermediate coverage,

and two SAMs at a high coverage. BDA preferentially adsorbs to step edges, elbows and fcc sites of the Au(111) herringbone reconstructions. In addition, BDA is susceptible to tip-induced movement, which can potentially lead to applications in molecule manipulations. These investigations shed light on the high stability of amines in single molecule conductance measurements using gold contacts.

3.2. Introduction

3.2.1. Introduction to SAMs

The field of self-assembled monolayers (SAMs) on surfaces has developed rapidly since Nuzzo and Allara reported the adsorption of alkanethiols onto gold in 1983[1] and still remains a hot topic due to its important applications in nanotechnology. As the thinnest organic films, SAMs offer the possibility of design and functionality control on the surface patterning at the nanometer scale, which can be tailored by using different organic molecules and surfaces. SAMs can be fabricated into nanoscale patterns in numerous ways, such as by scanning probes, microcontact printing, and particles beam (photons, electrons and ions, neutral atoms) [2-6].

The most widely studied SAM system is thiols/thiolates[2, 7-12] on gold due to its stability. In contrast, studies on amines SAMs on gold are sparse, mostly due to the weak interaction between amines and gold. In early studies, it was shown that alkenes terminated with amines either do not form stable monolayers on Au(111) by solution-

based adsorption method[7] or only form a weak monolayer that can be easily displaced by a trace of polar impurities[13, 14]. More recently, Xu et al. demonstrated that $H_2N(CH_2)NH_2$ forms a stable, ordered SAM on the Au surface from its vapor phase[15]. Lee et al. used liquid/solid phase STM to study the coadsorbed film of aniline and solvent molecules on an Au(111) electrode in perchloric acid and benzenesulfonic acid[16-18]. Dell'Angela et al. reported a well ordered SAM formed by vapor deposition of a few amines, including BDA molecules, as probed by UPS, XPS and NEXAFS [19].

3.2.2. Introduction to the Break-junction Conductance Measurement

Since the introduction of a single molecule as an active electronic component[20], efforts have been devoted to measurements of single-molecule transport properties[21-23]. Although the concept seems simple, this goal has proven difficult to achieve. One of the biggest obstacles is that the conductance measurement of a single molecule typically exhibits large variations. In 2006, Venkataraman et al. used a so-called "modified STM" to demonstrate the possibility of achieving reliable and reproducible conductance values for molecules with amine groups [24-26].

Single molecules were used to form in metal-molecule-metal junctions in their measurement (Figure 3.1) between an Au tip and Au surface. The Au surface was first flamed and annealed with butane and then covered with molecules (either in a solution form or a dry form). Then the Au tip was crashed into and pulled back from the Au

surface in a controlled way. Since the surface is covered with molecules, there is a high chance for a molecule to be picked up by the tip and trapped between the tip and the surface, thus forming a metal-molecule-metal junction. By measuring the I-V curve of the junction, they were able to determine the existence of such a junction.

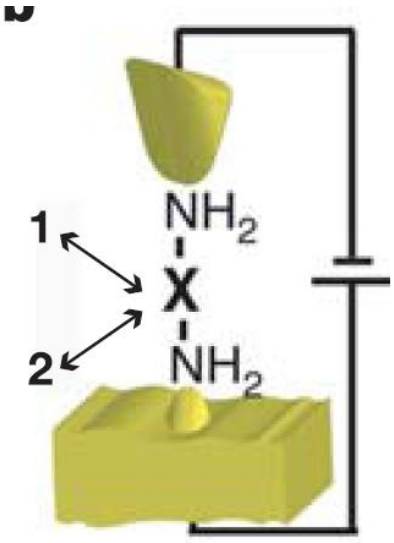

Figure 3.1: Schematic of the modified STM in Venkataraman's measurements. [24]

By Crashing the Au tip into the Au surface covered by amines and pulling back the tip for a few angstroms, a relatively stable metal-molecule-metal junction is formed.

When a clean Au surface without any molecules is used, the conductance exhibits a step-wise decrease with steps being at integral multiples of $G_0 = 2e^2/h$, the quantum conductance of a single-channel ballistic junction. Below G_0, the conductance either

decreases exponentially due to tunneling between two electrodes or drops directly below the experiment detection limit, possibly due to the relaxation of Au atom chains (Figure 3.2a, yellow traces). However, when a molecule is trapped between the Au electrodes, the conductance measurement exhibits additional steps. In their experiment, the conductance of several classes of molecules was measured, including diamines, dithiols, and diisonitriles. From the conductance measurements shown in Figure 3.2a, we can see that the traces of BDA (blue traces) have more stable values compared with the other two molecules. The authors also constructed conductance histograms of the bare surface and three different molecules using more than 3000 traces without any data selection or processing. The result in Figure 3.2b clear indicates that BDA has a much better-defined peak than the other two molecules.

The authors attributed the stable conductance to a more uniform configuration of the amines bound to the Au surfaces, as formed between electron lone pairs of nitrogen and gold adatoms. DFT calculations also confirm the conclusion by providing a model with an amine group sitting on top of a gold adatom [19, 27-29].

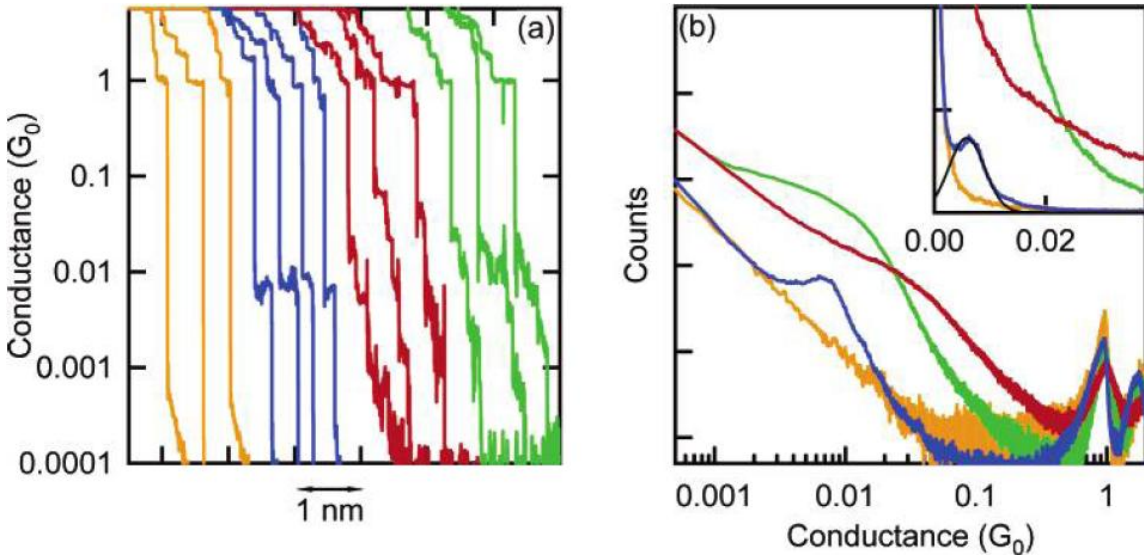

Figure 3.2: Conductance measurement of clean Au, BDA, 1,4-benzenedithiol (BDT), and 1,4-benzenediisonitrile (BDI) in Venkataraman's measurements. [26]

(a) Samples conductance traces with clean Au (yellow), BDA (blue), BDT (red), and BDI (green) in a semi-log plot. (b) Conductance histograms of the same molecules with the same color scale in a log-log scale. The inset shows the same histograms in a linear scale.

3.2.3. Introduction to 1,4-benzenediamine (BDA)

BDA, a model diamine compound, is composed of a benzene ring and two amine groups in the para position. Its Synonyms include 1,4-benzenediamine, 1,4-diaminobenzene, 1,4-Phenylenediamine, or p-phenylenediamine. It is used as a component of engineering polymers and composites, aramid fibers, rubber chemicals, textile dyes and pigments[30]. BDA possesses many outstanding properties, including high temperature stability, high strength, and chemical and electrical resistance.

At room temperature, BDA is a colorless solid when pure; however, it can become yellowish or pinkish when it is oxidized, which is the basis for its application in dyes and hair colorants[31]. The physical properties of BDA are listed in Table 1.

Table 1: Selected physical properties of BDA

Molecular weight	Boiling point (760 mmHg)	Melting point (760 mmHg)	Vapor pressure (25°C)	Vapor pressure (25°C)	Vapor Density (Air=1)
108.1	271 °C	139-142 °C	<0.0001 mmHg	0.08 mmHg	3.7

BDA has two isomers: cis and trans forms, depending on the relative orientation of the NH_2 groups with respect to the plane of the aromatic ring. In the cis form, both the NH_2 groups are on the same side of benzene ring (Figure 3.3b); in the trans form, the amine groups are on different sides of the benzene ring (Figure 3.3c). Different studies at different environments show different ratios of cis vs. trans forms: ab initio calculations[32, 33] and dipole moment measurement[34] show a mixture of both forms in the gas phase; X-ray crystallography measurement[35] shows a trans configuration in the crystal structure.

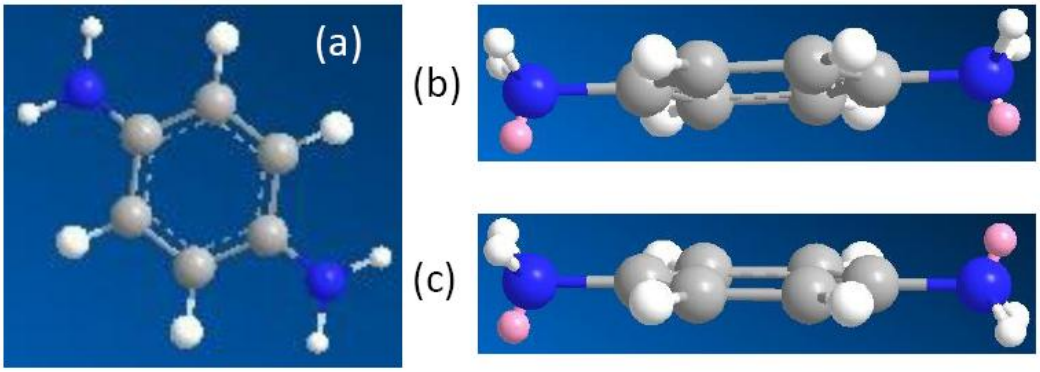

Figure 3.3: Diagrams of BDA and two isomers.
(a) 2D diagram of BDA. (b-c) 3D diagrams of (b) cis form and (c) trans form of BDA. Grey: carbon atoms; blue: nitrogen atoms; white: hydrogen atoms; pink: electron lone pair.

When amine compounds are deposited to Au surface, DFT calculations [19, 29] reveal three interesting conclusions: 1) the binding energy of all possible geometries of amine/Au is considerably lower than that for thiols. 2) The largest binding energy is obtained at the situation when amines sit directly above an Au adatom (atop position), which is in the range from 0.3eV to 0.53eV. 3) When BDA is adsorbed on the Au(111) flat surface at relatively high coverage, the calculated binding energy is 0.36eV and the calculated angle between the benzene ring and the surface is about 27^{o}, which means the molecule is not lying flat but rather tilting up from the surface at high coverage. This phenomena has been supported by NEXAFS measurement[19].

Due to lack of extensive studies of SAMS formed with amines, a detailed picture of the amine/gold bonding is still missing. In this chapter, we provide topographic images of 5

phases of BDA molecules on Au(111), including 3 phases of BDA SAMs, at different coverages obtained with ultrahigh vacuum (UHV) scanning tunneling microscope (STM). In addition, we report on the preferential adsorption of BDA on reconstructed Au(111) surface and tip-induced movement of BDA.

3.3. Experiment Methods

Our experiments were performed using a low-temperature STM (Omicron LT-STM) under UHV condition at a base pressure of $3x10^{-11}$ Torr. Clean Au(111) substrates were obtained by repeated cycles of Ar-ion sputtering and thermal annealing at 900K. 1,4-bezenediamine (BDA) with purity >99% was commercially purchased from Sigma-Aldrich and adsorbed to the surface by vapor deposition through a leak valve in the chamber (See Chapter 1). An appropriate vapor pressure of the BDA molecules was achieved by heating the solid source to 100^{o}C and then reduced to a desired vapor pressure at the vacuum chamber by controlling the opening of the leak valve.

We deposited the molecules on the surface held at both room temperature and a reduced temperature. For the reduced temperature deposition, the sample was transferred directly from a liquid-helium cooled stage and exposed while held on a room-temperature holder. In order to keep temperature comparable for each deposition, the deposition time was maintained at 5 minutes for all exposures. As a result, we were able to vary the surface coverage of BDA by means of controlling the sample temperature (either room temperature or a reduced temperature) as well as the BDA vapor pressure inside the

vacuum chamber upon deposition. All the STM measurements were performed at liquid helium temperature (5K).

3.4. Results and Discussion

3.4.1. Morphology of BDA on Au(111)

Phase diagram

By varying the coverage of BDA on Au(111), we observed 5 different surface phases of the adsorbed molecules on Au(111) (see Figure 3.4), including 3 phases of SAMs. The different phases are: (1) isolated BDA molecules (at very low coverage), (2) a chain structure (at low and intermediate coverage), (3) a network structure (at intermediate coverage), (4) a fully-covered line lattice (at high coverage), and (5) a fully covered square lattice (at high coverage). We designated the first two as flat BDA molecules and the latter three as SAMs.

Very low coverage (~0.007 Langmuir)

In the very low coverage regime (Figure 3.4a), BDA molecules are well isolated from one another. From our STM images, the coverage is estimated to be 0.007 Langmuir based on the Au atom density on the surface.

Shown in Figure 3.5(a) is an STM image of individual BDA molecules after deposition. The measured height is about 1 Å above the Au clean surface. Each BDA molecule assumes a spindle shape. It also exhibits two elongated tails on opposite sides, which correspond to the amine groups. A line profile is shown across the long side of the molecule in Figure 3.5(b). The length corresponding to the white line in the topographic image is approximately 9Å; the transverse dimension (red line) is ~ 7Å. The shape and height of BDA do not change with the polarity of the sample bias.

As a comparison, the nitrogen to nitrogen distance is about 5.6 Å in one molecule in the gas phase [35, 36]. It appears that the dimension of the BDA molecules measured by STM is about 3 Å larger than the nominal N-N distance. There are two possible reasons: 1) the charge transfer between the molecules and the surface leads to a localized electronic density around the molecule; 2) the image is broadened by the tip. In principle, we should be able to determine the tip sharpness by a sharp object on the surface, e.g. the edges. However, the edges are also covered by the molecules, which make it difficult to estimate the tip dimension.

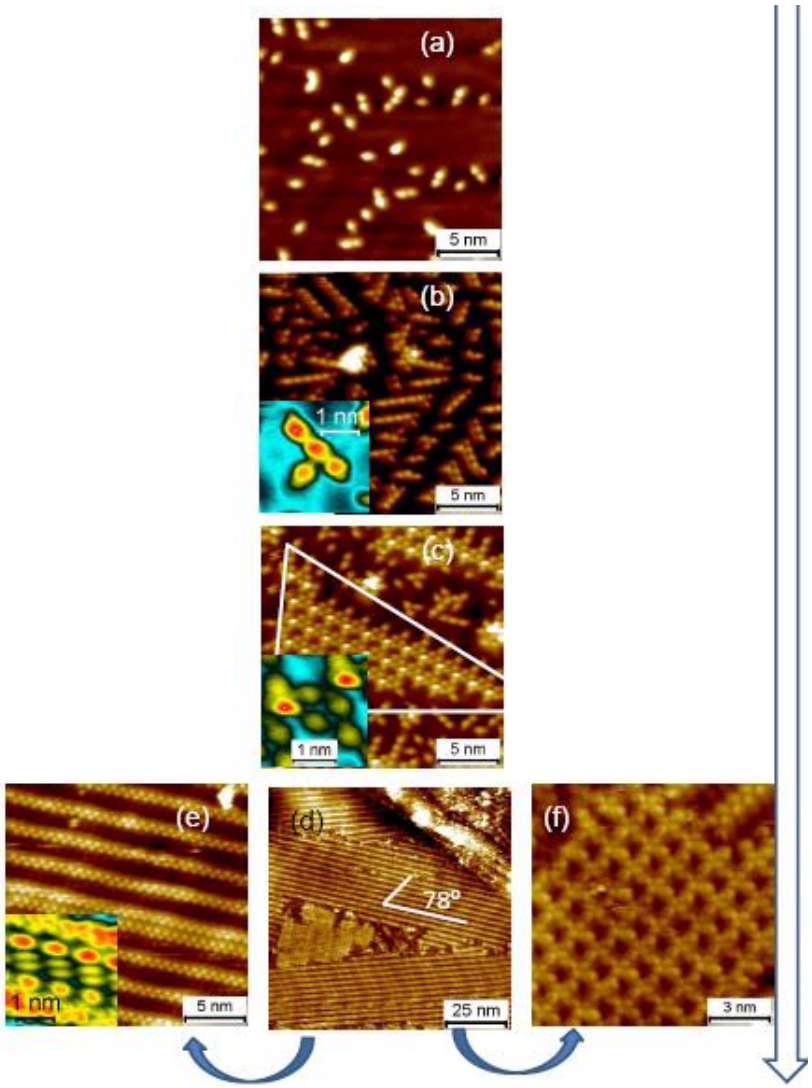

Figure 3.4: STM topographic images of BDA on Au(111) at different coverages.

Coverage increases from (a) to (d). (a) Very low coverage: isolated BDA molecules. (b) Low coverage: chain structures. (c) Intermediate coverage: coexistence of line structure and network structure. (d) High coverage. (e) and (f) are high resolution images of two phases of high coverage: fully-covered line lattice and square lattice. The insets of (b) and (c) are high resolution images of the line structure and the network structure. The inset of (e) shows the structure between bright lines.

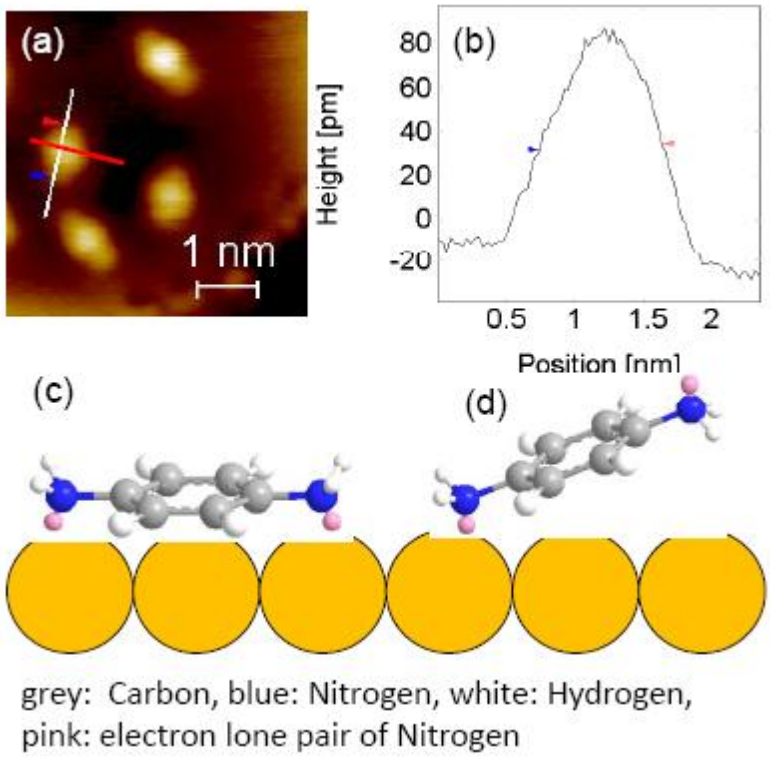

Figure 3.5: Experimental results and models of individual BDA molecules on the Au(111) surface.

(a) An STM image of an individual BDA molecule on Au(111) surface at 5K (b) Line profile along the white line on BDA. The scanning condition is 0.04V, 5pA. (c-d) Models for BDA: (c) cis form and a flat geometry and (d) trans form and a tilted geometry.

Figure 3.5 (c-d) illustrate structural diagrams for the two conformational BDA isomers: the cis and trans forms, as defined by the relative orientation of the NH_2 groups with respect to the plane of the aromatic ring, with their respective possible geometries on the Au(111) surface. In the cis form, both the NH_2 groups are on the same side of benzene ring with the electron lone pairs of amines interacting with the gold atoms, and thus

form donor-acceptor bonds. At the same time, the carbon may also bond to the gold atoms with van der Waals force. In the trans form, the amine groups are on different sides of the benzene ring and the only possible interaction is through the Nitrogen electron lone pairs. Our STM images show a rather symmetric geometry of an individual BDA molecule with a protruded center and two tails on each side, indicating a cis configuration with both of the amine groups facing down and lying flat on the surface.

Previous theoretical and experimental studies about BDA molecules have shown different results of BDA forms. Ab initio calculations[32, 33] and dipole moment measurement[34] show a mixture of both cis and trans forms in the gas phase. However, X-ray crystallography measurement[35] show only a trans form in the crystal structure.

We have also studied the preferred adsorption sites for BDA molecules on the Au(111) surface. They are found to be the step edges, herringbone elbows, and the fcc herringbone terraces.

In Figure 3.6(a), we see directly that BDA adsorbs at the step edges even at very low coverage. By comparing the molecules at different locations, BDA at the edges appear smaller, probably due to stronger bonding with Au atoms at the edges. In Figure 3.6(b), since the underlying herring reconstruction of Au(111) is clearly visible, it is easy to distinguish the fcc and hcp regions. (See Chapter 2 for more detailed introduction.) At very low coverage like Figure 3.6(b), BDA molecules only occupy the fcc sites and the elbow sites on the terraces. More experiments are needed in order to determine which site out of the three has the largest binding energy.

If we compare the numbers of BDA molecules on the hcp sites and the fcc sites (estimated to be approximately 1:30), we can estimate the adsorption energy difference of BDA molecules at these sites by:

$$\frac{P_1}{P_2} = e^{-\Delta E/kT} \tag{3.1}$$

Where P_1 and P_2 are the BDA molecule number density on hcp sites and fcc sites, respectively, T is the temperature when the molecules are frozen, which we assume is 100K. ΔE is the adsorption energy difference. As a result, ΔE ~0.02eV.

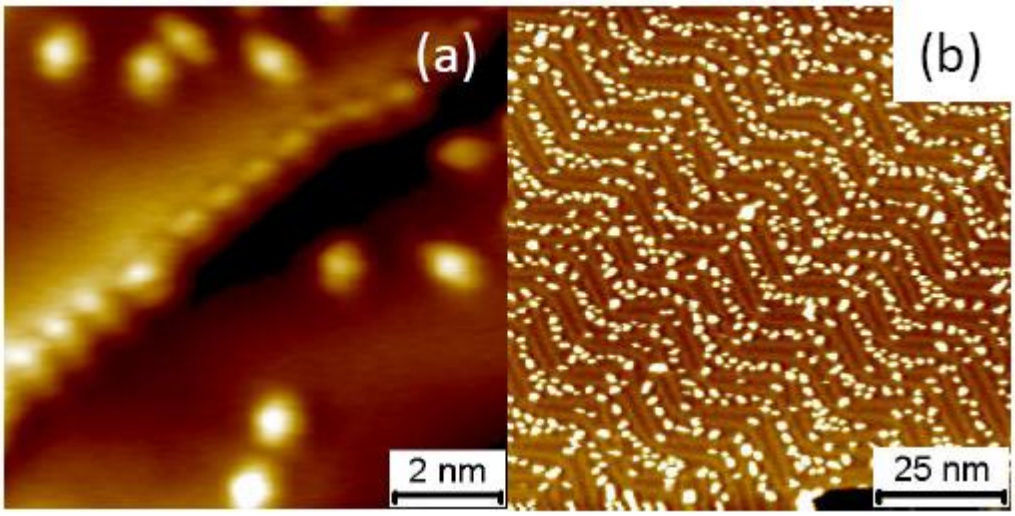

Figure 3.6: STM images of the preferred adsorption sites of BDA molecules.

STM shows preferred adsorption sites at (a) step edges, (b) herringbone elbows and fcc sites at very low coverage. The images were taken at sample bias of 0.04V-0.1V.

Low coverage case (~0.02 Langmuir)

In the low coverage regime (~0.02 Langmuir), BDA molecules start to connect in lines. As the inset of Figure 3.4b shows, the tails of BDA are off the axis of the BDA lines by approximately 30^{o}, and the spacing between the nearest low points is about 8 Å,. Sometimes, BDA molecules also attaches to the line from a branch site. We designated this type of structure as the branched chain structure.

Furthermore, we can also observe that the adsorbed BDA molecules generally follow a pattern that resembles a herringbone structure. At such coverage, the reconstruction is hard to resolve while imaging the BDA layer. We could, however, scan the same area separately at different bias to obtain both the BDA structures (low bias) and the underlying Au(111) herringbone structure (high bias). As a result, we can identify the different stacking regions in Figure 3.7a. The dark regions are herringbone ridges and the blue arrows indicate the fcc sites. We can deduce that at low coverage, the BDA molecules can adsorb on both fcc and hcp sites of the Au(111) herringbone reconstruction but not on the ridge sites.

In order to understand the chain structure, we can refer to BDA molecules in the crystal form where the molecules are coordinated by hydrogen bonds[37, 38] from a nitrogen atom of one BDA molecule to a hydrogen atom of an amine group of another BDA molecule[35]. We propose that adsorbed BDA molecules also interact with each other by means of hydrogen bonding. The 30^{o} off-axis orientation of BDA molecules in the line structure and the slightly smaller spacing between BDA molecules in the chain

structure than the length of an individual BDA molecule support this hypothesis. More specifically, we propose the following model: An amine group of one BDA has two hydrogen atoms, one of which interacts with nitrogen of an amine group of another BDA, whose hydrogen atom can interact with a third BDA. That's how a line forms. In addition, the fourth BDA can also interact with the rest of the hydrogen atom of the amine group from a branch site. Figure 3.8 shows a crude 2D diagram of the model.

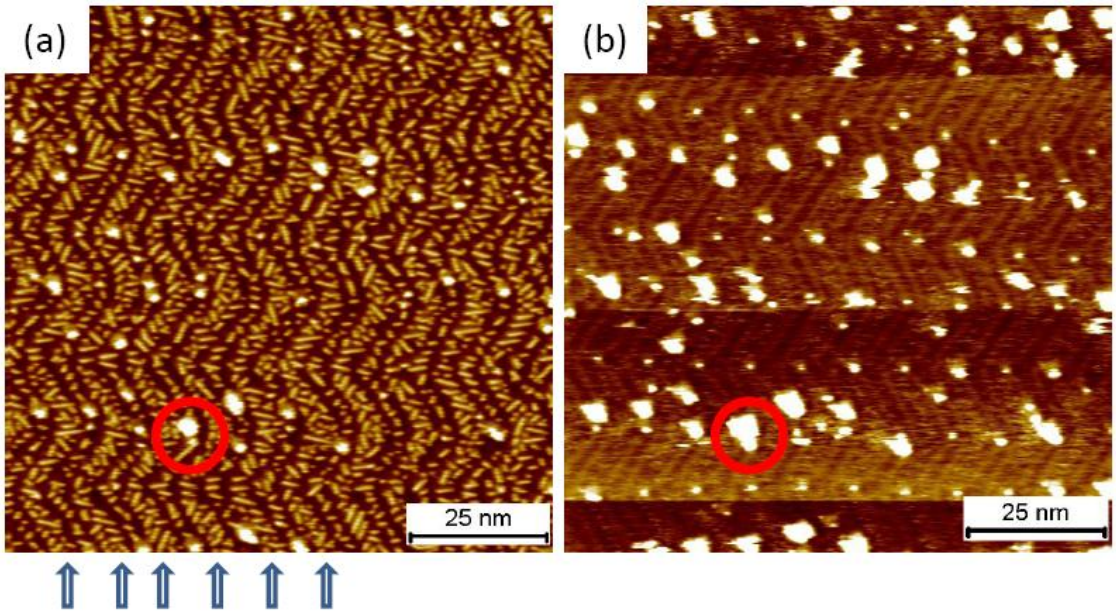

Figure 3.7: STM images of the preferred adsorption sites of BDA chain structures at low coverage.

The same area STM images taken at different bias show different features: (a) intact chain structures at a sample bias of 0.1V; and (b) Au(111) herringbone structure with a few decorations at a sample bias of -1.5V. In (a), the dark regions are herringbone ridges. The fcc sites of the underlying Au(111) herringbone structure are marked with the blue arrows. The same impurity was marked with red circles as a reference in both images.

Figure 3.8: Diagram of BDA molecule in the line structure.
The molecules on the line connect to each other with hydrogen bonds between hydrogen atoms and nitrogen atoms. The BDA orientation is approximately 30^{o} with respect to the axis of the line of molecules (in red line). It can also connect to the line from a branch site, also via a hydrogen bond.

The explanation of the preferential adsorption to the step edges and the elbow sites is straight forward as amines like to bind to coordinatively unsaturated sites [19, 26] such as step edges and herringbone elbow sites[39]. As for the preference with fcc sites over hcp sites, a similar preference has been observed for thiolates on Au(111) [9, 40], in which case, DFT calculation [41] found out that Au-Au vertical distances around the fcc sites elongate by a significant distance upon thiolate adsorption and relaxation propagates to the second layer, while there is a weaker effects in hcp configuration. As a

result, the binding energy of thiolates on fcc sites is about 0.24eV greater than hcp sites. We believe that similar interpretation also applies to this situation, though further studies, especially theoretical calculation, are needed.

Intermediate coverage case (~0.06 Langmuir)

As the coverage increases, 3 different forms of BDA SAMs were observed. At intermediate coverage (~0.06 Langmuir), there is a coexistence of a new SAM phase (the network structure) as well as the chain structure found at lower coverage. The network structure appears with a white triangle in Figure 3.4c. A close-up image of one unit cell is shown in the inset of Figure 3.4c. Each unit cell is composed of 6 BDA molecules. One spot or a 0.5 Å greater apparent height structure is observed. It is unclear whether this is a topographic effect or an electronic effect, both of which could contribute to the change in apparent height.

We also studied the preferred adsorption sites of the network structure. With the same method as in the previous section, we were able to identify the different stacking regions in Figure 3.9a where the dark regions are herringbone ridges and the blue arrows show the fcc sites. Thus we deduce that the network structures preferentially adsorb to the fcc elbow sites.

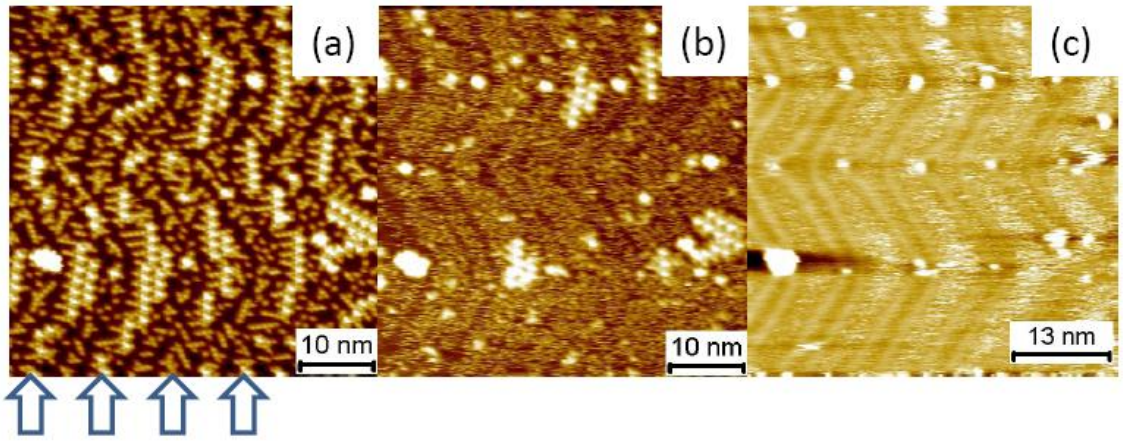

Figure 3.9: STM images of the preferred adsorption sites of BDA network structures.

The same area STM images taken at different bias show different features: (a) intact network structures and chain structures at a sample bias of 0.1V; (b) partially destroyed BDA structures with a faint Au(111) herringbone structure background at a sample bias of 0.5V; and (c) Au(111) herringbone structure with a few decorations at a sample bias of -2V. In (a), the fcc sites of the underlying Au(111) herringbone structure are marked with the blue arrows.

High coverage (>0.1 Langmuir)

When the surface is fully covered, there is a coexistence of two phases: a line lattice (Figure 3.4d) and a square lattice (Figure 3.4e). The line lattice covers the majority of the surface. In this case, the bright lines are composed of a zigzag pattern of bright spots and have a periodic distance of 3nm in the direction perpendicular to the lines. The spacing is about 8 Å between the two bright spots along the line and 6 Å across the line. The underlying herringbone arrangement of the reconstructed Au(111) surface is also visible on the covered surface. The angle between herringbone bridge ($[11\bar{2}]$) and the

bright line is about 68°. The inset of Figure 3.4d shows that the entire surface, not just the region of the more pronounced lines, is covered. In addition, the height difference between the bright spots and the fine structure spots in the dark areas is around 1 Å, which is less than the height difference for an additional layer of BDA molecules. This height difference could be induced by different tilting angles of the adsorbed BDA molecules. The other fully-covered BDA SAM, the square lattice, has a four-fold symmetry with 2 nm periodicity in both directions.

When the coverage increases, more intermolecular interaction causes the BDA molecules to stack on the surface with a more upright position, which may cause different tilting angles of BDA, which makes a small height difference of about 1 Å. Larger tilting angle due to higher coverage has been observed for thiols SAMs on Au(111) [11]. XPS study of BDA on polycrystalline Ni surface indicates a coexistence of tilted BDA and flat BDA at a low coverage [33]. Moreover, the tilting angle has been theoretically reported by DFT calculation for amine on Au[29], particularly of BDA[19] as well. An NEXAFS study also confirms the average tilting angle of BDA on Au(111)[19].

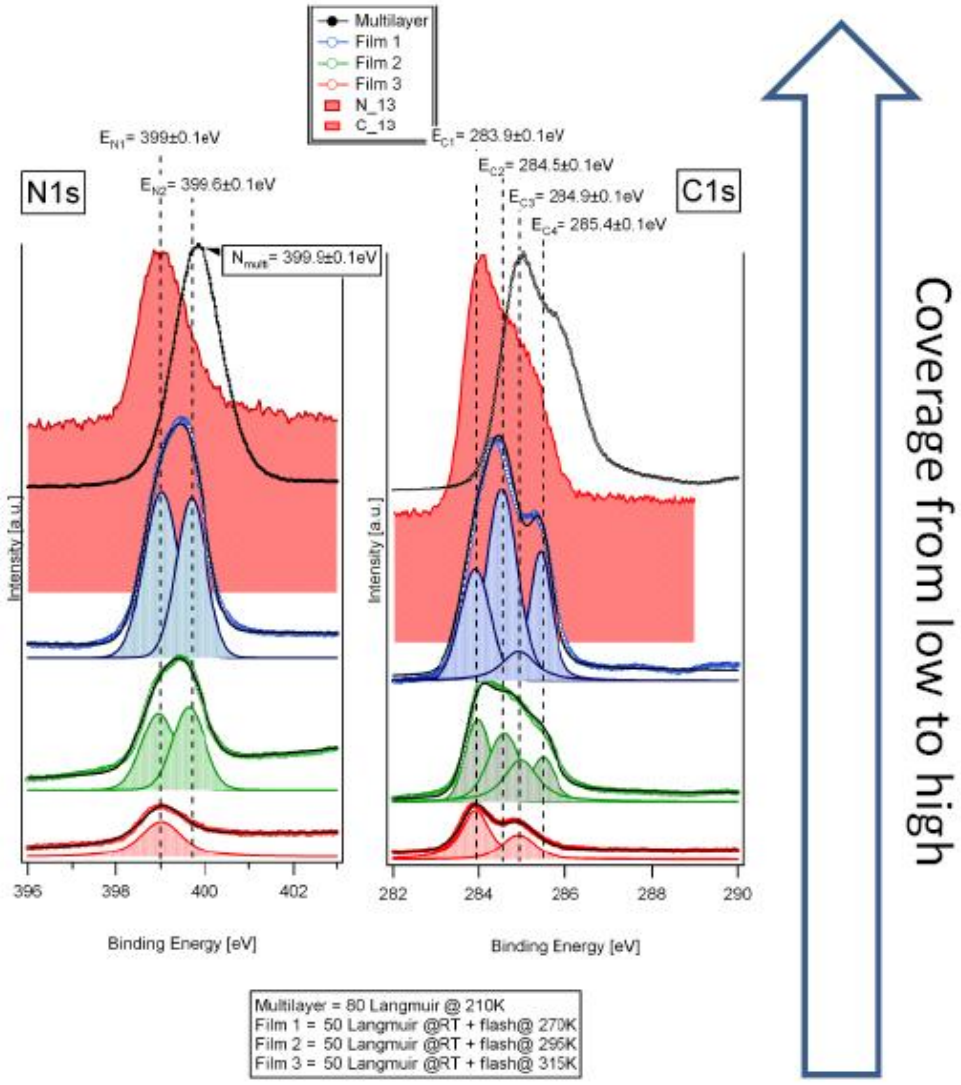

Figure 3.10: XPS spectra of N 1s and C 1s of BDA on Au(111) form a low to high coverage.

(a) N1s peaks of BDA molecules on Au(111), with coverage increasing from the bottom to the top. At a low coverage, only one peak exists; at a higher coverage, there are two peaks; at multilayer coverage, only the second peak is left. (b) Corresponding C1s peaks of BDA on Au(111).

An independent XPS study (Figure 3.10) shows the transition of N 1s peak from a low coverage to multilayer coverage. The data exhibit only one N 1s peak at a low coverage, indicating a flat BDA geometry in a cis form. If the BDA molecules are tilted on the surface or having a trans form, there should be at least two different N peaks, one for the N interacting with Au and the other is not. As the coverage increases, another N 1s peak appears at higher energy. The intensity of this peak continues to increase until it becomes the sole peak for multilayer coverage. The emergence of the 2 peaks implies that the BDA molecules start to stand up from the surface or stack on each other in a flat geometry. The former situation was confirmed by the same authors using NEXAFAS [19]. This phenomenon is consistent with our STM images at different coverages. At multilayer coverage, XPS can only detect the top few layers. As a result, only one peak exists for multilayer coverage.

3.4.2. Tip-induced movement of BDA on Au(111)

In our measurement, we also found out that the BDA molecules are extremely sensitive to the scanning conditions. For stable imaging, we were constrained to bias voltages below 100meV with a current of 5pA.

If the sample bias was increased without changing the current, those isolated molecules and the chain structures were not visible whereas the network structure still remained intact. If we scanned the same area at a higher bias, the molecules were found to be

disturbed and reorganized on the surface. There was no evidence of fragmentation of the BDA molecules induced by the STM. This process is shown in Figure 3.11a-e.

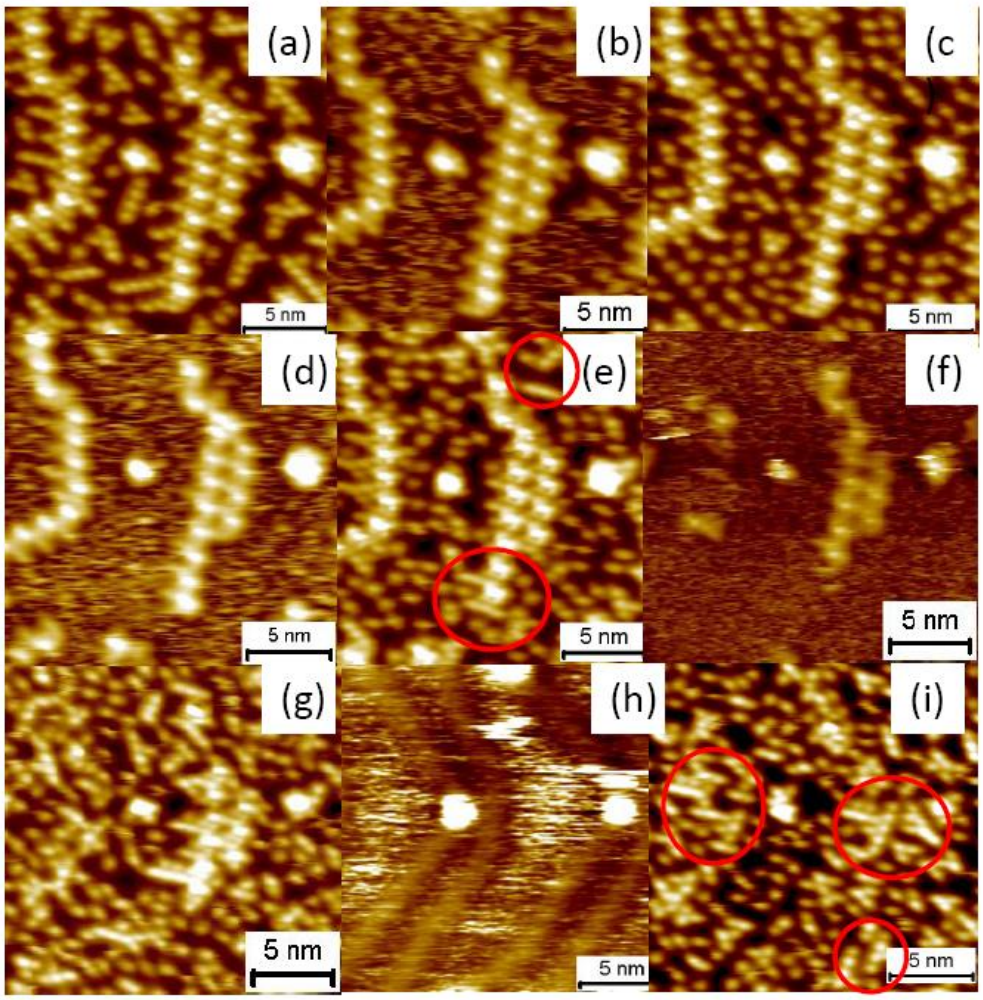

Figure 3.11: Sequential STM images of the same area under different bias voltage and current.

Scanning conditions of sequential STM images are (a) 0.1V, 5 pA; (b) 0.5V, 5 pA; (c) 0.1V, 5 pA; (d) 2V, 5 pA; (e) 0.1V, 5 pA; (f) 2V, 500 pA; (g) 0.1V, 5pA; (h) -2V, 5 pA; (i)0.1V, 5 pA. The red circles indicate the new lines formed after disturbance by the STM tip.

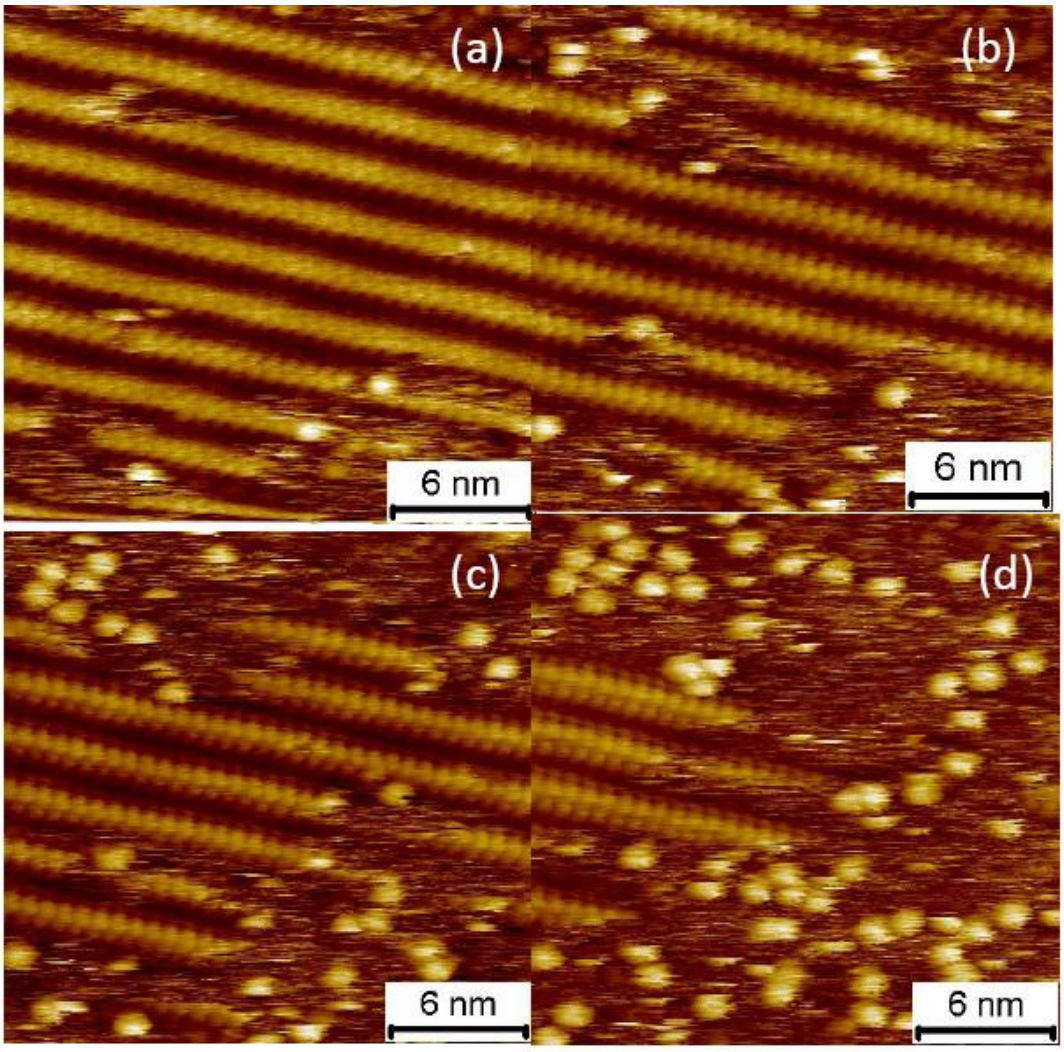

Figure 3.12: Sequential STM images of the same area of the line lattice.

The ordered line lattice is disturbed during scanning at U= -2.5V and I=200pA.

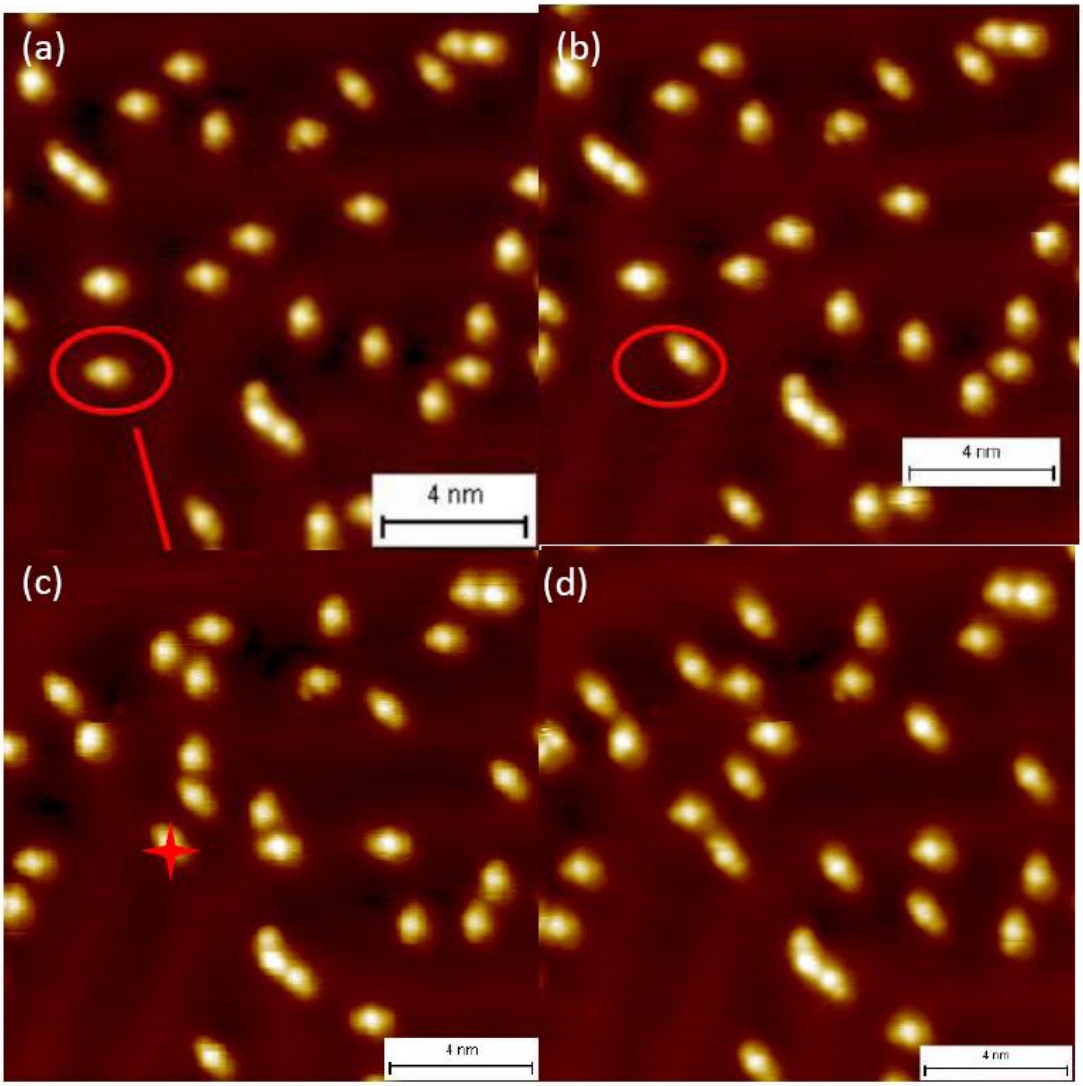

Figure 3.13: Sequential STM images of the same area before and after a voltage pulse.

(a-b): STM image before and after application of a voltage pulse of 1V. (c-d): STM image before and after voltage pulse of 2V. The red circles and the red star indicate the location where the pulse was applied. The scanning condition is U=40meV and I=3pA.

With the same sample bias, but at a different current, the result was also different. Figure 3.11f is the STM image with the sample bias of 2V and current of 500pA, the network structure started to melt. The image taken afterwards (Fig 3.11g) also confirmed that result.

The surface was scanned at a sample bias of -2V in Fig 3.11h. No BDA molecules could be resolved at this condition, but instead the underlying Au(111) herringbone could be observed. A scan afterwards indicated that most of the BDA molecules were scattered and reorganized on the surface, forming a few new lines in Fig 3.11i.

The fully-covered line lattice and square lattice were also unstable for scanning at $\pm 2V$ as Figure 3.12 shows.

At a very low coverage, the molecules remain stable on the surface at bias voltage of 40meV and current of 3pA. However, if a voltage pulse is applied at the surface, the BDA will diffuse to another location within 1-2nm or rotate. When a voltage of 1V is applied, only the BDA molecule where the pulse was applied would move; when a voltage of 2V is applied, tens of BDA of a larger range of ~5nm would diffuse (Figure 3.13).

There are two possible causes for the migration of BDA under scanning at high bias. It could be due to the tip-induced electrical field or tip-induced vibrational excitation.

In order to discuss the tip-induced electrical field, we have to examine how close the tip is located near the sample in our case. Combining the Landauer theory of the conductance quantum and the quantum square lattice tunneling model, we can obtain the

tip-sample distance is roughly $z \approx 6\,\mathring{A}$ with scanning conditions of U=0.1V and I=5pA. If the bias voltage is increased to 1V without changing the current, $z \approx 7\,\mathring{A}$. The tip-sample distance was confirmed in STM measurements.[42-44]

If we use a rough estimation of $E = U / z$, the electric field is apparently increased largely by increasing the bias from 0.1V to 1V. In the real STM imaging condition, due to the asymmetrical geometry, the electric field is inhomogeneous and concentrated in the vicinity of the tip. With a similar tip-sample distance and a bias of 1 to 10V, the electrical field strength is in the range of from 0.2 to $2\,V/\mathring{A}$ by simulation.[42]

Tip-induced BDA migration can be discussed in terms of the potential energy difference of BDA in the electric field. As a first order approximation,

$$\vec{p} = \vec{\mu} + \alpha \vec{E}, \qquad (3.2)$$

where $\vec{\mu}$ is the permanent dipole moment, α is the field-induced polarizability of the adsorbate. In the case of BDA, the calculated static dipole moment is 2.49D for the cis, and 0 for the trans conformer[32]. As a result, the potential energy is given as

$$U(\vec{r}) = -\vec{\mu} \bullet \vec{E}(\vec{r}) - \frac{1}{2}\alpha E^2(\vec{r}). \qquad (3.3)$$

With only static dipole moment considered, the consequential potential energy of BDA cis form is about 0.1-1.0eV. This result is confirmed by experiment (1.0eV with Helium atom spectroscopy measurement[19]) and the DFT calculation (0.1-0.4eV [19, 29]).

Since the diffusion energy of an adsorbate on a metal surface is about 1/10~1/3 of the binding energy [45, 46], then the diffusion energy of BDA on Au(111) is about 0.01-0.3eV, which is comparable with the tip-induced electric potential energy of BDA. Similar STM observations of tip-induced atoms or molecules movement due to electrical field effect have been reported [42-45, 47-50].

Another possible explanation of the BDA migration is the tip-induced vibrational excitation. According to Persson, et al. [51, 52], when the tunneling electron injects into the unoccupied states of an adsorbate, the molecule forms a temporary ionic state. When the electron then tunnels into the substrate, the molecule goes back to the electronic neutral state. During the process, the nucleus positions of the molecule could be changed due to the Coulomb potential changes and thus excites a vibration. After this, the vibrational excited state can decay with two channels. One is to decay directly to an electron-hole pair, the other is to decay into a low-frequency translational mode, which is associated with the lateral hopping of the molecules. Ab-initio calculations[32] demonstrated that the stretch mode of N-H in BDA is about 0.4eV. STM measurement with ammonia on Cu(111)[53] also reported that inelastic tunneling electron introduced by STM tip is capable of the excitation of the N-H stretch mode, $\nu_s(N-H)$ in ammonia with 408meV.

However, this vibrational excitation usually exhibits a sharp increase of the incident rate (defined as the percentage of the adsorbates that moved after a voltage pulse) around the excitation energy[27], whereas our measurement indicates a gradual increase of moving

of BDAs with increasing bias above 0.1V. In addition, one voltage pulse can result in tens of BDAs moving which is much bigger than the range an excited electron can influence. Therefore, we conclude that the first explanation is more plausible for the movement of BDA due to higher bias scanning above 0.1V.

3.5. Summary

In summary, We observed 5 different phases of BDA structures on Au(111) with UHV STM: isolated BDA, chain structure, network structure, line lattice, and square lattice. The latter three are SAMs. A simple phase diagram of different patterns due to different coverages is provided. In our studies, isolated BDA adsorbs flat to the surface with a cis configuration. In addition, we also showed the preferred adsorption sites of BDA, including step edges, herringbone elbow sites and fcc sites. Finally we also observed that BDA can be easily disturbed by the tip-induced electric field and hop to 1-2nm away.

3.6. Bibliography

1. Nuzzo, R.G. and D.L. Allara, *Adsorption of bifunctional organic disulfides on gold surfaces.* Journal of the American Chemical Society, 1983. **105**(13): p. 4481-4483.

2. Love, J.C., et al., *Self-Assembled Monolayers of Thiolates on Metals as a Form of Nanotechnology*. Chemical Reviews, 2005. **105**(4): p. 1103-1170.

3. Ginger, D.S., H. Zhang, and C.A. Mirkin, *The Evolution of Dip-Pen Nanolithography.* Angewandte Chemie International Edition, 2004. **43**(1): p. 30-45.

4. Krämer, S., R.R. Fuierer, and C.B. Gorman, *Scanning Probe Lithography Using Self-Assembled Monolayers.* Chemical Reviews, 2003. **103**(11): p. 4367-4418.

5. Liu, G.-Y., S. Xu, and Y. Qian, *Nanofabrication of Self-Assembled Monolayers Using Scanning Probe Lithography.* Accounts of Chemical Research, 2000. **33**(7): p. 457-466.

6. Xia, Y., et al., *Unconventional Methods for Fabricating and Patterning Nanostructures.* Chemical Reviews, 1999. **99**(7): p. 1823-1848.

7. Bain, C.D., J. Evall, and G.M. Whitesides, *Formation of monolayers by the coadsorption of thiols on gold: variation in the head group, tail group, and solvent.* Journal of the American Chemical Society, 1989. **111**(18): p. 7155-7164.

8. Esplandiú, M.J., H. Hagenström, and D.M. Kolb, *Functionalized Self-Assembled Alkanethiol Monolayers on Au(111) Electrodes:1. Surface Structure and Electrochemistry.* Langmuir, 2001. **17**(3): p. 828-838.

9. Fitts, W.P., J.M. White, and G.E. Poirier, *Low-Coverage Decanethiolate Structure on Au(111): Substrate Effects.* Langmuir, 2002. **18**(5): p. 1561-1566.

10. Fitts, W.P., J.M. White, and G.E. Poirier, *Thermodynamics of Decanethiol Adsorption on Au(111):Extension to 0 ^{o}C.* Langmuir, 2002. **18**(6): p. 2096-2102.

11. Poirier, G.E., W.P. Fitts, and J.M. White, *Two-Dimensional Phase Diagram of Decanethiol on Au(111).* Langmuir, 2001. **17**(4): p. 1176-1183.

12. Cyr, D.M., B. Venkataraman, and G.W. Flynn, *STM Investigations of Organic Molecules Physisorbed at the Liquid-solid Interface.* Chemistry of Materials, 1996. **8**(8): p. 1600-1615.

13.Bigelow, W.C., D.L. Pickett, and W.A. Zisman, *Oleophobic monolayers : I. Films adsorbed from solution in non-polar liquids.* Journal of Colloid Science, 1946. **1**(6): p. 513-538.

14. Bigelow, W.C., E. Glass, and W.A. Zisman, *Oleophobic monolayers. II. Temperature effects and energy of adsorption.* Journal of Colloid Science, 1947. **2**(6): p. 563-591.

15. Xu, C., et al., *Molecular interactions between organized, surface-confined monolayers and vapor-phase probe molecules. 6. In-situ FT-IR external reflectance spectroscopy of monolayer adsorption and reaction chemistry.* Analytical Chemistry, 1993. **65**(15): p. 2102-2107.

16. Chen, S., et al., *In Situ STM Elucidation of the Adsorption and Polymerization of Alkyl Ring-Substituted Aniline on Au(111) Electrode.* The Journal of Physical Chemistry C. **114**(18): p. 8493-8499.

17. Lee, Y., et al., *In Situ STM Revelation of the Adsorption and Polymerization of Aniline on Au(111) Electrode in Perchloric Acid and Benzenesulfonic Acid.* Langmuir. **26**(8): p. 5576-5582.

18. Yau, S., et al., *Structures of Aniline and Polyaniline Molecules Adsorbed on Au(111) Electrode: as Probed by in Situ STM, ex Situ XPS, and NEXAFS.* The Journal of Physical Chemistry C, 2009. **113**(31): p. 13758-13764.

19. Dell'Angela, M., et al., *Relating Energy Level Alignment and Amine-Linked Single Molecule Junction Conductance.* Nano Letters. **10**(7): p. 2470-2474.

20. Aviram, A. and M.A. Ratner, *MOLECULAR RECTIFIERS.* Chemical Physics Letters, 1974. **29**(2): p. 277-283.

21. Reed, M.A., et al., *Conductance of a molecular junction.* Science, 1997. **278**(5336): p. 252-254.

22. Porath, D., et al., *Direct measurement of electrical transport through DNA molecules.* Nature, 2000. **403**(6770): p. 635-638.

23. Cui, X.D., et al., *Reproducible measurement of single-molecule conductivity.* Science, 2001. **294**(5542): p. 571-574.

24. Venkataraman, L., et al., *Dependence of single-molecule junction conductance on molecular conformation.* Nature, 2006. **442**(7105): p. 904-907.

25. Venkataraman, L., et al., *Electronics and Chemistry:Varying Single-Molecule Junction Conductance Using Chemical Substituents.* Nano Letters, 2007. **7**(2): p. 502-506.

26. Venkataraman, L., et al., *Single-Molecule Circuits with Well-Defined Molecular Conductance.* Nano Letters, 2006. **6**(3): p. 458-462.

27. Bilic, A., et al., *Adsorption of ammonia on the gold(111) surface.* Journal of Chemical Physics, 2002. **116**(20): p. 8981-8987.

28. Li, Z. and D.S. Kosov, *Nature of well-defined conductance of amine-anchored molecular junctions: Density functional calculations.* Physical Review B, 2007. **76**(3): p. 035415.

29. Hoft, R.C., et al., *Adsorption of Amine Compounds on the Au(111) Surface: A Density Functional Study.* The Journal of Physical Chemistry C, 2007. **111**(37): p. 13886-13891.

30. Dupont. [cited 2011 01.07]; Available from: http://www2.dupont.com/Specialty_Chem_Intermediates/en_US/products/ppd.html.

31. Smiley, R.A., *Phenylene- and Toluenediamines.* Ullmann's Encyclopedia of Industrial Chemistry. 2000: Wiley-VCH Verlag GmbH & Co. KGaA.

32. Tzeng, W.B. and K. Narayanan, *Excited-state structure and vibrations of p-diaminobenzene studied by ab initio calculations.* Journal of Molecular Structure: THEOCHEM, 1998. **434**(1-3): p. 247-253.

33. Lindell, L., et al., *Characterization of the interface dipole at the paraphenylenediamine-nickel interface: A joint theoretical and experimental study.* Journal of Chemical Physics, 2005. **122**(8): p. 12.

34. McClellan, A.L., *Tables of Experimental Dipole Moments.* W.H. Freeman and Company, 1964.

35. Colapietro, M., et al., *Molecular structure of p-diaminobenzene in the gaseous phase and in the crystal.* The Journal of Physical Chemistry, 1987. **91**(7): p. 1728-1737.

36. Oezel, A.E., S. Akyuez, and J.E.D. Davies, *Structural investigation of 1,4-diaminobenzene complexes of nickel and cadmium chloride by FT-IR and Raman spectroscopy.* Journal of Molecular Structure, 1995. **348**: p. 77-80.

37. Emsley, J., *Very strong hydrogen bonding.* Chemical Society Reviews, 1980. **9**(1): p. 91-124.

38. Fuller, W., *Hydrogen Bond Lengths and Angles Observed in Crystals.* The Journal of Physical Chemistry, 1959. **63**(10): p. 1705-1717.

39. Chambliss, D.D., R.J. Wilson, and S. Chiang, *Nucleation of ordered Ni island arrays on Au(111) by surface-lattice dislocations.* Physical Review Letters, 1991. **66**(13): p. 1721.

40. Maksymovych, P. and J.T. Yates, *Au Adatoms in Self-Assembly of Benzenethiol on the Au(111) Surface.* Journal of the American Chemical Society, 2008. **130**(24): p. 7518-7519.

41. Grönbeck, H., A. Curioni, and W. Andreoni, *Thiols and Disulfides on the Au(111) Surface: The Headgroup - gold Interaction.* Journal of the American Chemical Society, 2000. **122**(16): p. 3839-3842.

42. Yazdani, A., D.M. Eigler, and N.D. Lang, *Off-Resonance Conduction Through Atomic Wires.* Science, 1996. **272**(5270): p. 1921-1924.

43. Akiyama, R., T. Matsumoto, and T. Kawai, *A Scanning Tunneling Microscopy Study of Electrostatic and Proximity Effects in Tip-Assisted Migration and Desorption of a DNA Base Molecule on SrTiO3.* The Journal of Physical Chemistry B, 1999. **103**(29): p. 6103-6110.

44. Akiyama, R., T. Matsumoto, and T. Kawai, *Mechanism of tip-assisted migration and desorption of DNA base molecules on an $SrTiO_3$ surface.* Applied Physics A: Materials Science & Processing, 1998. **66**(0): p. S719-S722.

45. Stroscio, J.A. and D.M. Eigler, *Atomic and Molecular Manipulation with the Scanning Tunneling Microscope.* Science, 1991. **254**(5036): p. 1319-1326.

46. Nilekar, A.U., J. Greeley, and M. Mavrikakis, *A Simple Rule of Thumb for Diffusion on Transition-Metal Surfaces.* Angewandte Chemie, 2006. **118**(42): p. 7204-7207.

47. Tsong, T.T., *Effects of an electric field in atomic manipulations.* Physical Review B, 1991. **44**(24): p. 13703.

48. Tsong, T.T. and C.-S. Chang, *High Field Effects and Methods Useful for Transferring Atoms in Scanning Tunneling Microscope.* Japanese Journal of Applied Physics, 1995. **34**(Part 1, No. 6B): p. 3309.

49. Whitman, L.J., et al., *Manipulation of Adsorbed Atoms and Creation of New Structures on Room-Temperature Surfaces with a Scanning Tunneling Microscope.* Science, 1991. **251**(4998): p. 1206-1210.

50. Saranin, A.A., et al., *Growth of thallium overlayers on a Si(100) surface.* Physical Review B, 2005. **71**(3): p. 035312.

51. Komeda, T., et al., *Lateral Hopping of Molecules Induced by Excitation of Internal Vibration Mode.* Science, 2002. **295**(5562): p. 2055-2058.

52. Persson, B.N.J. and H. Ueba, *Theory of inelastic tunneling induced motion of adsorbates on metal surfaces.* Surface Science, 2002. **502-503**: p. 18-25.

53. Pascual, J.I., et al., *Selectivity in vibrationally mediated single-molecule chemistry.* Nature, 2003. **423**(6939): p. 525-528.

Chapter 4

Properties of Graphene Nanoislands on Co(0001)

Graphene, as a 2D material, has attracted a lot of attention due to its novel properties since the successful fabrication in 2004. The high carrier mobility[1, 2], possibility of chemical doping[3, 4], and optical transparency make it a potential building block for the future devices[5], such as touchscreens, liquid crystal displays, organic photovoltaic cells, and organic light-emitting diodes (OLEDs). In addition, its weak spin-orbit coupling and large phase coherence length have suggested graphene as an ideal material for spintronics application [6-8].

In order to make devices out of graphene, it is inevitable to make metal electrodes connected with it, which can alter its electronic properties. Hence, it is essential to understand the interaction between graphene and metal in the contact region.

4.1. Introduction

4.1.1. Introduction to Graphene and Graphene Nanoribbons

Brief history of graphene

The term, "graphene", was first coined to describe a single sheet of graphite in graphite intercalation compounds in 1987 [9]. However, it was not a true 2D material then, in the sense that it is neither in a free-standing form nor supported by a weak-coupled substrate. In 2004, Andre Geim and Konstantin Novoselov first successfully separated a single layer sheet of graphene on SiO_2, who were awarded the 2010 Nobel Prize in Physics[10]. Since its discovery, graphene has become a popular subject due to its novel properties.

One definition of graphene is described as follows: "Graphene is the name given to a flat monolayer of carbon atoms tightly packed into a two-dimensional (2D) honeycomb lattice, and is a basic building block for graphitic materials of all other dimensionalities. It can be wrapped up into 0D fullerenes, rolled into 1D nanotubes or stacked into 3D graphite"[11]. Indeed, graphene is the mother of all graphitic materials. Besides the materials mentioned in the definition, it can also be etched into nanoribbons, which will be discussed further later. The carbon-carbon bond length in the honeycomb lattice of graphene is 1.4 Å.

Fabrication methods

The primary methods to fabricate graphene are drawing method and epitaxial growth method (on SiC, Cu, Ni, Co, etc).

Drawing method refers to repeated splitting of a graphite piece into increasingly thinner pieces until a thin enough piece is achieved. It is often called the scotch tape method as scotch tape is used to separate the layers. One of the most common substrate used is SiO_2 due to its wide application in the semiconductor industry and the weak coupling with graphene. In many cases, a special thickness of 300nm of SiO_2 is used in order to increase the contrast between graphene and the underlying substrate under optical microscope. With this method, graphene with extremely high mobility can be obtained. However, graphene size and throughput are limited in this case.

Epitaxial growth method refers to the use of the atomic structure of various substrates to seed the graphene growth. The commonly used substrates are SiC or metal (Cu, Co, and Ir). With SiC, a direct heating (>1100^{o}C) of SiC can produce graphene[12], whereas in the case of metal substrates, a chemical vapor deposition procedure is needed with hydrocarbon precursors[13, 14]. With this method, the graphene size can be as large as the substrate. However, the graphene thickness might be not uniform and the interaction between the graphene and substrate can influence the graphene properties.

There are also other ways to produce graphene. For example, graphene can be produced through reduction of graphite oxide, which can be traced back to 1962 by P. Boehm[15]. By rapid heating of graphite oxide, few percent of graphene flakes can be produced along with graphite powders. However, the quality of the graphene flakes are not as good as exfoliated graphene.

Selected properties and potential application of graphene

Graphene has unique transport properties due to its band structure. Intrinsic graphene is a semi-metal or a semiconductor with zero bandgap. The energy dispersion relation E vs. k is linear for low energies near the six corners of the 2D Brillouin zone. Thus, electrons or holes with low energy near those conical corners behave like massless Dirac fermions and those six corners of Brillouin zone are called Dirac points. The linear dispersion relation can be expressed as:

$$E(\vec{k}) = \hbar \nu_F k \,, \tag{1.1}$$

Where ν_F is the Fermi velocity and ν_F ~10^6 m/s.

Experimental results show that graphene has remarkably high electron mobility at room temperature. It is also independent of temperature between 10K~100K, which implies that the dominant scattering mechanism is defect scattering [1, 16, 17].

Graphene is also an ideal material for spin transport due to its weak spin-orbit coupling, large phase coherent length and near absence of nuclear magnetic moments. Electron spin-current injection and control in graphene was recently demonstrated [6, 8, 18].

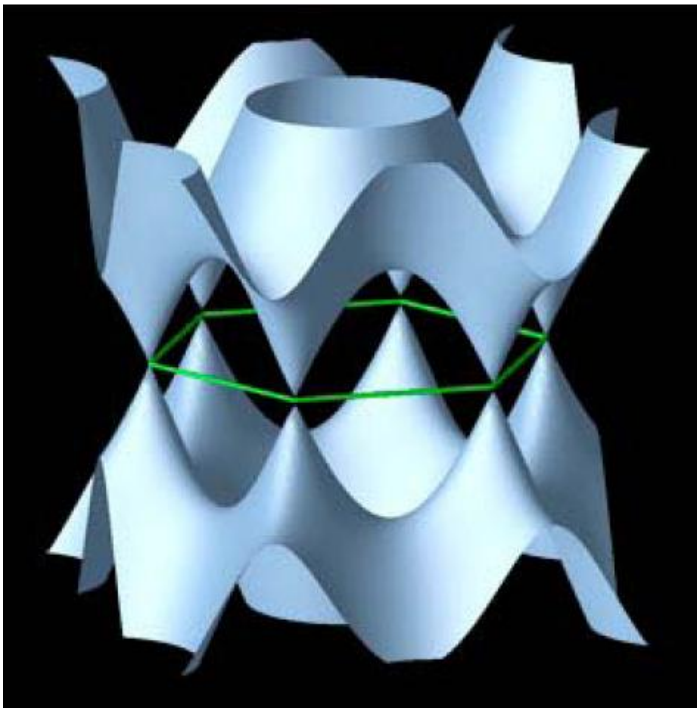

Figure 4.1: Schematic of the band structure of graphene near Fermi level.

The valence and conduction bands are connected by 6 Dirac points which are connected with green lines. The dispersion relation near Dirac points is linear, which can be depicted by Dirac cones.
(http://www.mirc.gatech.edu/raghu/?page_id=166)

Graphene nanoribbons (GNRs)

Graphene nanoribbons are particular patterns that are cut from graphene. Depending on how the edges are cut, they can have either zigzag or armchair pattern. In Figure 4.2, if the edges of the graphene nanoribbons are cut along green lines, the edges have zigzag patterns; if the edges are cut along the purple lines, they have armchair patterns.

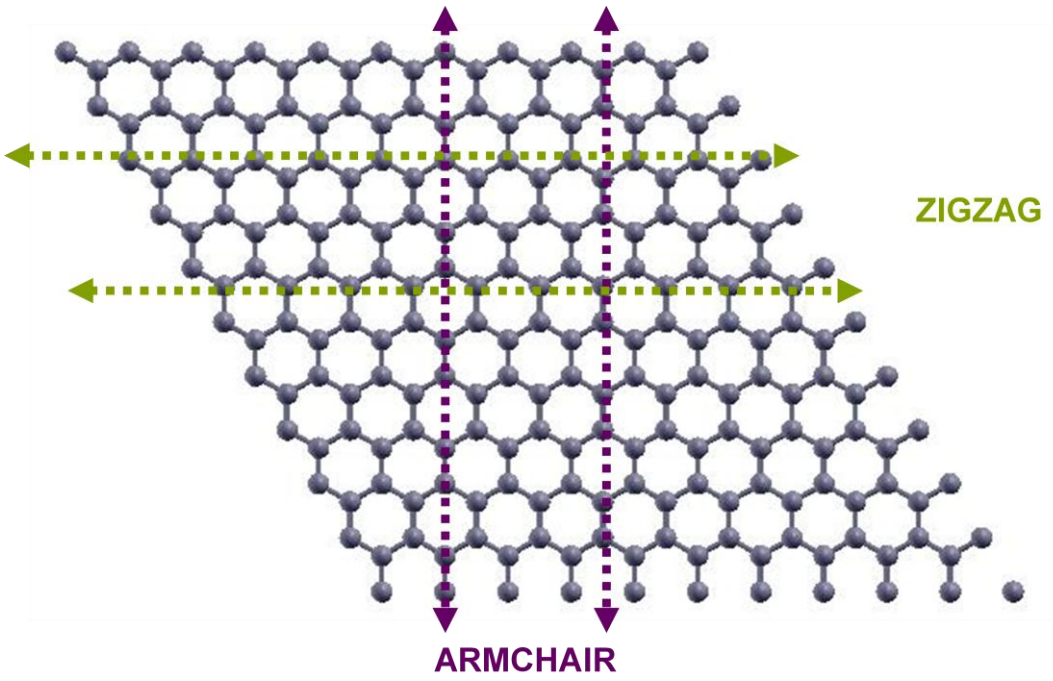

Figure 4.2: Schematic of the zigzag edges and armchair edges of graphene.

If the edges of the graphene nanoribbons are cut along green lines, the edges have zigzag patterns; if the edges are cut along the purple lines, they have armchair patterns. (Courtesy of Deborah Prezzi.)

Calculations based on density functional theory show that armchair GNRs are semiconductors with an energy gap proportional to the inverse of the width of GNRs[19], and zigzag GNRs are also semiconducting and present spin polarized edges. Transport measurement verifies the inverse relation between the energy gap and the GNR width[20] but no experiment before 2009 has identified the exact configuration at the edges[5]. The spin polarized edges make GNRs as a potential application in

spintronics. GNRs are also a possible alternative to copper as integrated circuit interconnects due to their high electrical and thermal conductivity.

4.1.2. Introduction to Cobalt (Co)

Cobalt properties

Cobalt is a strong ferromagnet, with a stable magnetic polarization and high orbital magnetic moment [5, 21-26], which makes it an ideal material for spintronics application[27]. Its Curie temperature is 1115^{o}C, and the magnetic moment is 1.6-1.7 Bohr magnetons per atom[28].

Cobalt is known to have two allotropic phases, an hcp phase (at low temperature) and an fcc phase (at high temperature). The transition between hcp phase and fcc phase is reversible but enthalpy change ($\Delta h \approx 440 kJ/mol$) and volume change ($\Delta V/V \approx 0.0036$) is small[24], this makes the intermix of the two crystal structure possible. The ideal transition temperature is approximately 700K with considerable thermal hysteresis.

When the transition happens, there is a substantial change in the stacking sequence. Hence, the electronic structure, electrical resistivity, and work function will also change [24, 29]. In this way, a single crystal Co sample might be destroyed when the transition happens, which make the sample preparation more difficult than gold preparation.

Co(0001) properties

As mentioned above, the stable structure of cobalt at room temperature is hcp structure, whose facet is conventionally described by a four-number miller index. The four unit vectors are shown in Figure 4.3 as $\vec{a}_1$, $\vec{a}_2$, $\vec{a}_3$, and $\vec{c}$, where $\vec{a}_1$, $\vec{a}_2$, and $\vec{a}_3$ are on the same plane and 120°C apart. $\vec{c}$ is perpendicular to all of the other unit vectors. In the four-number miller index for hcp structure, (ijkl), k=-(i+j).

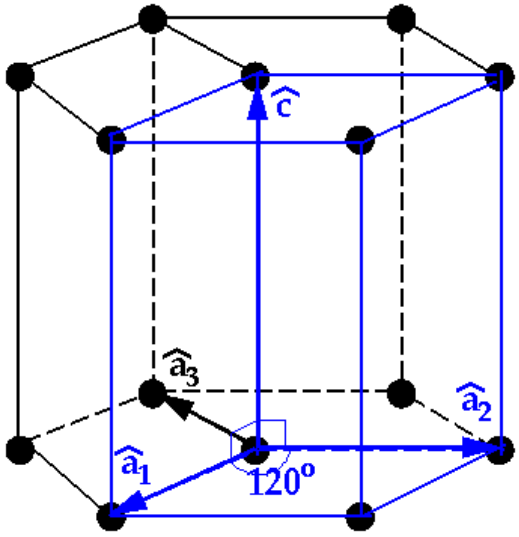

Figure 4.3: Schematic of the unit vectors in hcp crystals.

The four arrows indicate the four exes inside a unit cell of hcp crystals. $\vec{a}_1$, $\vec{a}_2$ and $\vec{a}_3$ are on the same place and 120° apart from each. $\vec{c}$ is perpendicular to all of the other axes.

(web.mse.uiuc.edu/courses/mse280/notes/03/ch3_p3.ppt**)**

The hcp(0001) has a ABA stacking order, shown in Figure 4.4(a). In any adjacent two layers, the atoms of one layer always occupy the hollow sites of the other layer, which is

identical to any two adjacent layers in the fcc(111) configuration. Only by adding at least one more layer can we distinguish between fcc(111) and hcp(0001)

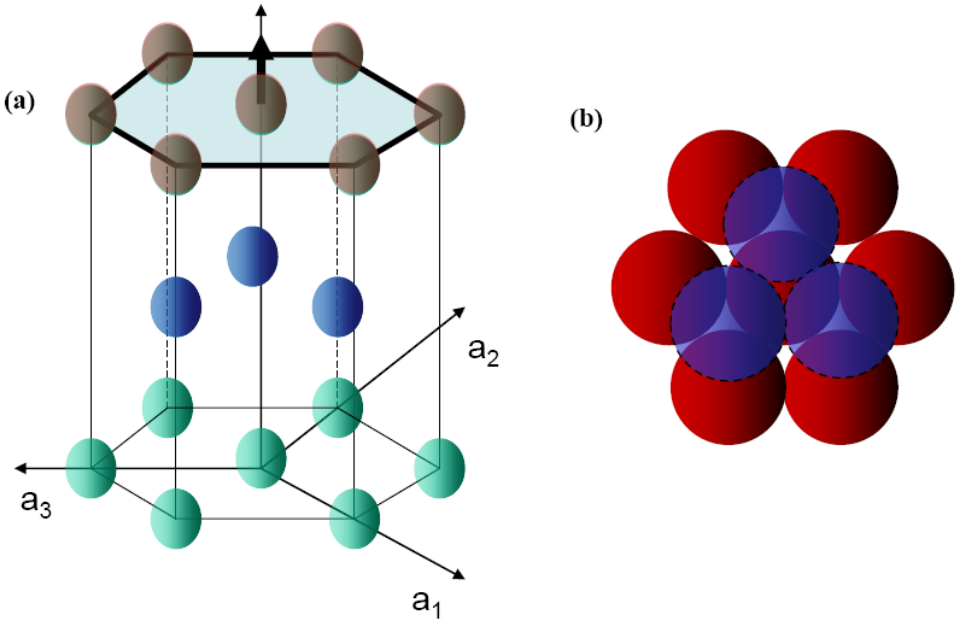

Figure 4.4: Schematic of hcp(0001) structures.
(a) The hcp structure from side view. Gery, blue and green atoms are in three different layers and form ABA stacking. (b) The same structure from top view. Blue and red atoms are two different layers.

(web.mse.uiuc.edu/courses/mse280/notes/03/ch3_p3.ppt**)**

From LEED studies, the Co(0001) atom-to-atom distance is ~2.5 Å. Compared with the graphene lattice constants, the mismatch is less than 2%. Besides, there is no indication of reconstruction and little surface relaxation, which suggest that we should observe 1x1 surface atoms without a long-range reconstruction[26, 30].

Preparation of Co(0001)

We use a traditional sputtering and annealing method, starting from a precut Co(0001) single crystal, similar to the preparation of Au(111). The most important difference is the annealing temperature. As mentioned in the previous section, there is a phase transition of Co hcp to fcc structure around 700K. Therefore, we have to strictly control the temperature below the transition temperature.

Electronic structures of Co(0001)

The electronic structures of Co(0001) have also been thoroughly studied. The origin of the states is mostly clear by combining experimental results (mainly obtained by photoemission spectroscopy and scanning tunneling spectroscopy) and theoretical calculations [21-23, 25, 26].

In the region of $E>E_F$, 3 peaks have been detected by spin-resolved inverse photoemission spectroscopy[23] within 2eV above Fermi level. The peak closest to the Fermi level is located at 0.24eV, which is assigned as a majority-spin surface state located at the surface Brillouin zone center $\bar{\Gamma}$. Another two features are around 0.75eV and are very close to each other. They are assigned to be associated with minority-spin states, and they are either surface states or a mixture of bulk states and surface states.

In the region below Fermi level, different measurements and calculations have some discrepancies. Photoemission spectroscopy detected a peak at -0.3eV, which was

assigned as a sp-like surface state [25, 26]. Scanning Tunneling microscopy detected a peak at -0.43eV instead and it was identified as a minority-spin $\bar{\Gamma}$-centered surface state[21]. Later on, a spin-polarized calculation identified an additional state at -0.5eV as a minority-spin surface state[22].

4.2. Experimental and Calculation Methods

The experiment was performed in a low-temperature Omicron STM under ultrahigh vacuum conditions, at a base pressure of $1x10^{-11}$ Torr. A cobalt single crystal with precut (0001) orientation was cleaned in situ by repeated cycles of argon sputtering and annealing at 570K. The STM image of a clean Co(0001) surface was shown in Figure 4.5 with no obvious reconstruction. The lattice constant is 2.5 Å, as expected[30].

After obtaining the clean surface, we dosed contorted hexabenzocoronene (HBC)[31] molecules (The structure of HBC was shown in the inset of Figure 4.5.) onto the clean Co(0001) surface (kept at room temperature) by thermal deposition at 605K. By annealing the sample at ~600K for 20min, we were able to obtain graphene nanoislands. All the STM and STS were performed at 4.9K.

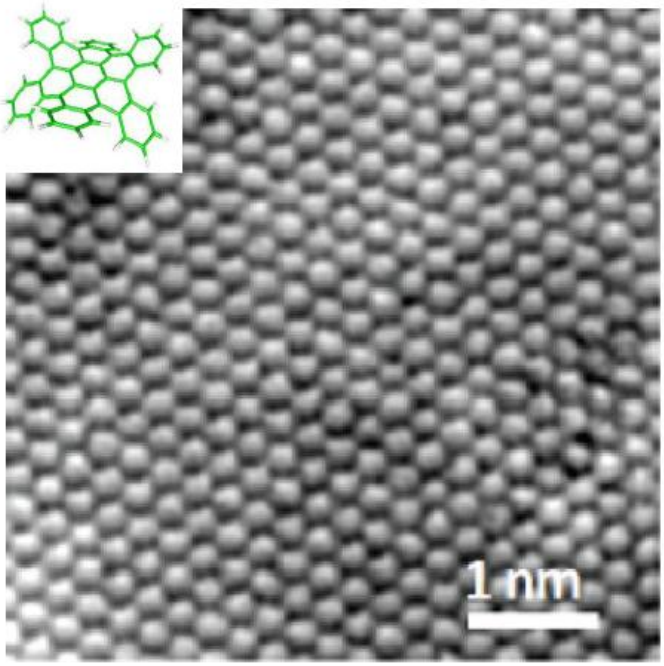

Figure 4.5: STM topographic image of Co(0001)

1x1 structure of Co(0001) without any obvious reconstruction. .The measured lattice constant is 2.5 Å. The scanning voltage is 5mV. The structure of one HBC molecule was illustrated in the inset.

We also carried out DFT calculations based on local-density approximation for the exchange-correlation potential, using a plane-wave basis set and ultrasoft pseudopotentials, as implemented in the Quantum-ESPRESSO package. The calculation was done by collaborators[5].

4.3. Results and Discussion

4.3.1 Structures of the Graphene Nanoislands

The STM images of as-deposited and after annealing HBC/Co(0001) are shown in Figure 4.6. The HBC molecules are clustered on the surface without any obvious ordered structures. After annealing at 600K, which is above the temperature (~410K) of dehydrogenation and H_2-desorption temperature for hydrocarbons on Co(0001)[32], they were dehydrogenated and epitaxially grow on the substrate to form islands of nanometer scale.

Most of the islands have triangular or hexagonal shape (shown in Figure 4.6b). All of the edges preferentially exhibit zigzag configurations which will be discussed in a later section. The measured height of the graphene adlayer above the metal surface varies with the scanning voltage, ranging from ~1.5 Å at low tunneling bias to ~2.2 Å at high tunneling bias (Figure 4.7).

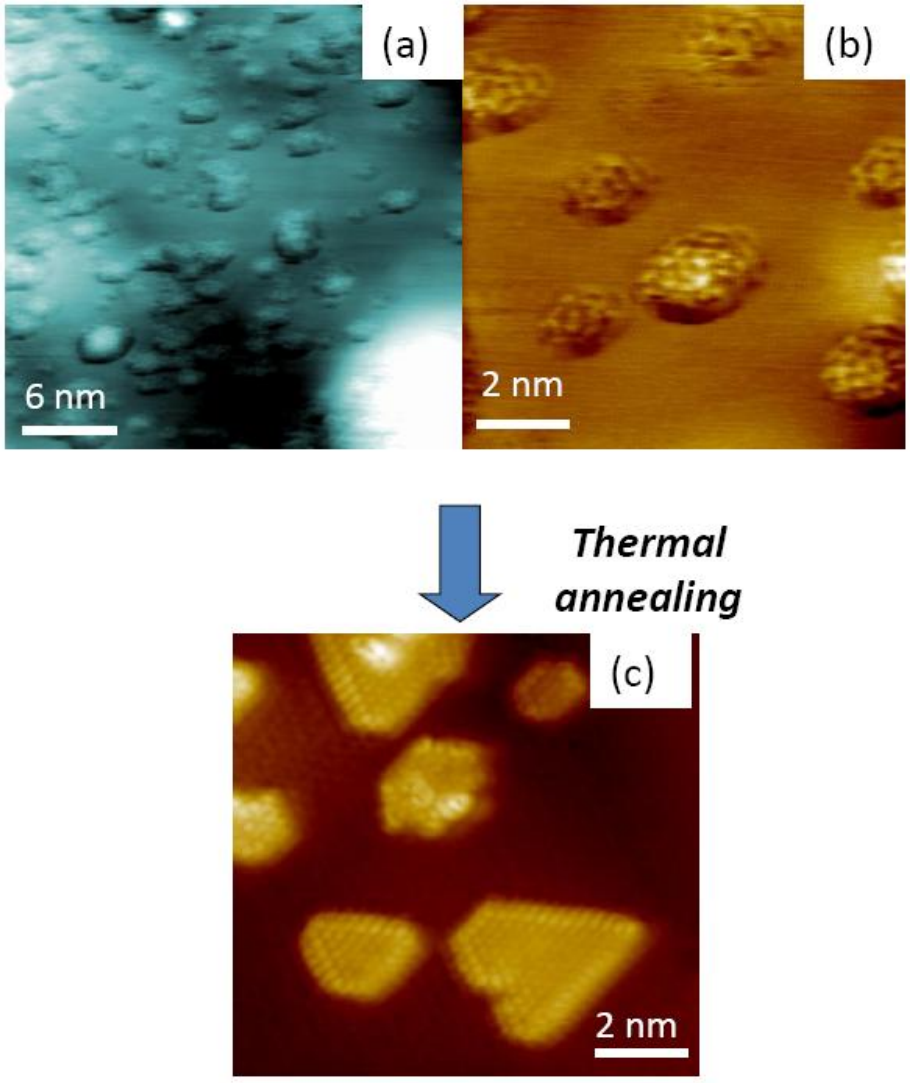

Figure 4.6: STM topographic images of as-deposited and after thermal annealing of HBC/Co(0001)

(a-b) Co(0001) after deposition of HBC molecules, which are clustered on the surface without ordered structures. After thermal annealing, they form triangular or hexagonal islands in (c). The scanning bias is 3mV in (a-b) and 5mV in (c).

We also examined the registry of the carbon atoms on the Co substrate. Under bias condition of -3mV, both the carbon atoms on the graphene adlayer and cobalt on Co(0001) are resolved, as in Figure 4.8. However, only every other carbon atoms are resolved, just like in the case of graphite[33]. This effect is expected due to the inequivalence of adjacent carbon atoms in the graphene adlayer with respect to the underlying substrate. With the help of the guidelines in Figure 4.8a, we can clearly see that the resolved carbon atoms are sitting directly above the cobalt atoms on the substrate (on-top site, or A-site), which demonstrates epitaxial growth of the graphene nanoislands. Since one of the two inequivalent carbon atoms in a graphene unit cell is sitting directly at A-site, the other carbon atoms must be either on an hcp hollow site (B-site), or on an fcc hollow site (C-site) of the cobalt substrate (See the AB and AC models in Figure 4.8b). Therefore, a structure model like the BC model in Figure 4.8b is unlikely.

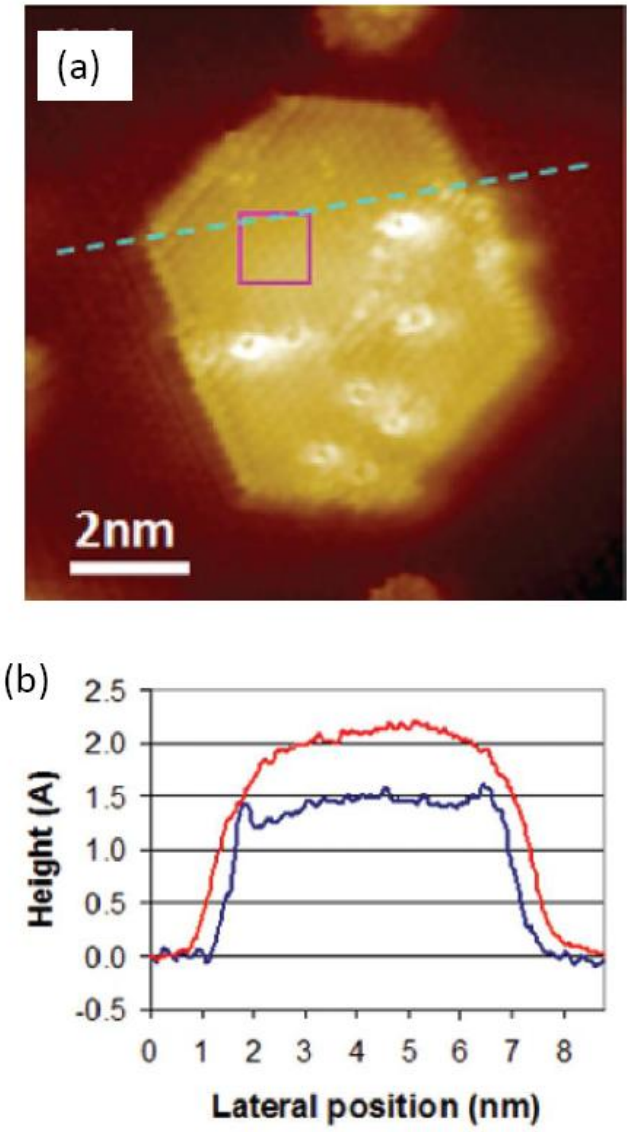

Figure 4.7: STM topographic image of one graphene island and the corresponding height profile on Co(0001)

In (a), an STM topographic image of one hexagonal-shape graphene island on Co(0001) is shown. Both of the carbon atoms on the graphene adlayer and the Co atoms on the substrate are resolved. The scanning voltage is -3mV. (b) The line profile at the light blue curve. The blue profile is from low bias scanning condition (-3mV) and the red profile is from high bias scanning condition (-400mV).

From DFT calculations, the spacing between the plane of Co atoms and the graphene adlayer for the on-top geometries was found to be 2.07 Å, which is comparable to the STM measurement of 1.5~2.2 Å. Comparing this spacing with those between graphene and other metals such as Au, Ag, Cu, or Pt which have a typical value of 3.3 Å[34], it is much smaller. This is due to a stronger interaction than van der Waals interaction with the surface.

In addition, the binding energies for the three different structure models are also calculated. The AC model appears to be the most stable configuration (E_b=0.264eV), which has almost the same binding energy of the AB model (E_b=0.256eV). The BC model has the smallest binding energy (E_b=0.056eV) and is unlikely a stable configuration if compared to the AC and BC models. Similar results are also obtained from other calculation[34].

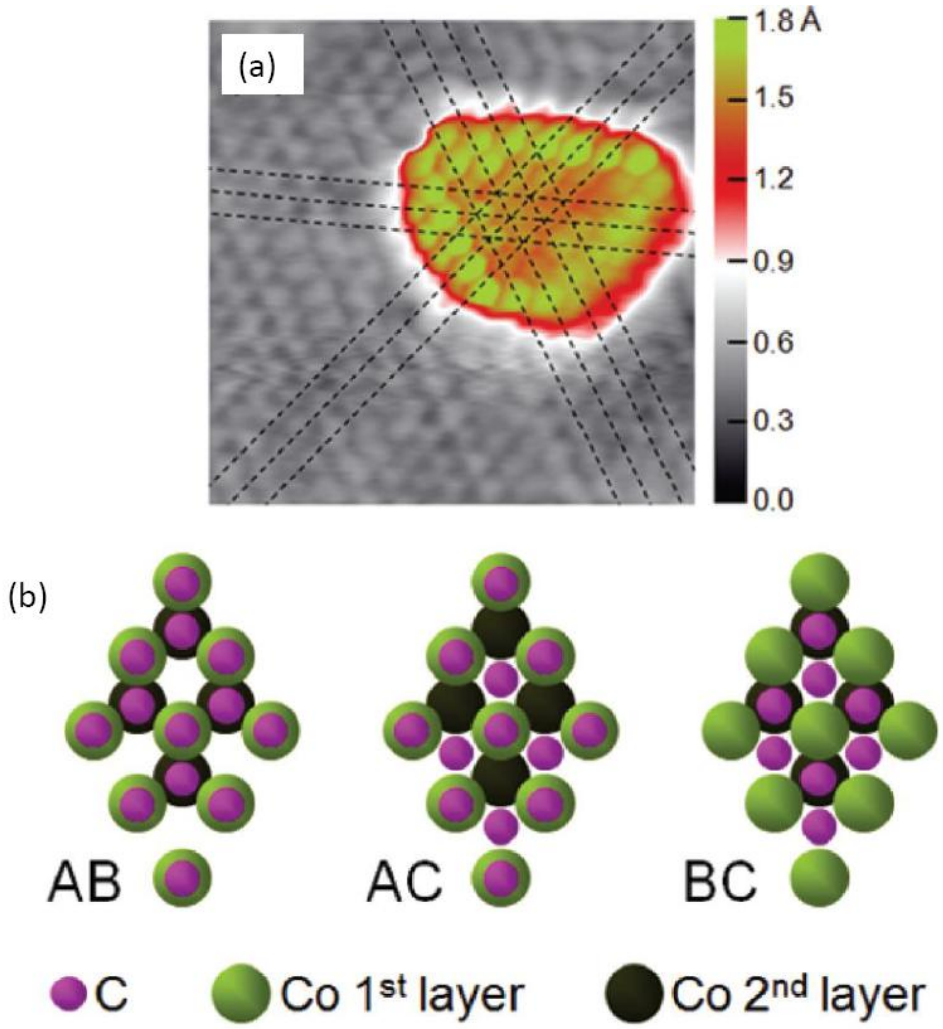

Figure 4.8: STM topographic image of one graphene island and the schematics of possible epitaxial growth models on Co(0001)

(a) An STM topographic image of one triangular graphene island on Co(0001). Both of the carbon atoms on the graphene adlayer and the cobalt atoms on Co(0001) are resolved under this tunneling condition. The registry of the carbon atoms relative to the substrate atoms are also shown with the guidelines. The scanning bias is -3mV. (b) Three structure models of epitaxially grown graphene on Co substrate are shown. Carbon atoms are shown in purple; the top layer and the second layer of Co atoms are shown in green and black, respectively.

4.3.2. Electronic Properties

The differential conductance spectra for both of the clean Co(0001) substrate and a graphene nanoisland on Co(0001) are shown in Figure 4.9. In the spectrum of cobalt in Figure 4.9a, we observe three main features: a strong peak at -0.52eV, a feature at +0.1eV, and a feature around +0.74eV. The peak at -0.52eV is found to be a Co(0001) surface state of minority-spin character, as expected from a theoretical calculation[22] The feature at +0.1eV is a majority-spin surface state at Brillouin zone center $\bar{\Gamma}$, to which similar results have been observed by photoemission measurement[23]. The feature around +0.74eV is associated with minority-spin, corresponding to either a surface state or a mixture of surface and bulk states[23].

The obtained STS spectra of the central region of the graphene nanoislands are very different from those of clean Co(0001). Shown in Figure 4.9b is the differential conductance spectrum averaged over a small area near the center of a graphene island (see the rectangular region in Figure 4.7a), well separated from the graphene boundaries and away from any defect. The results have been reproduced by different tips, therefore, we can rule out the contributions from tip artifacts. In addition, the grid points when the STS was performed encompass at least 23 graphene unit cells with a fine spacing of ~0.86 Å, therefore, the results represent true spatially averaged spectra over two atoms in the graphene unit cell. There are three main features on the spectra of graphene/Co at -0.37eV, 0.25eV, and +0.64eV. They are designated as P_1, P_2, and P_3, respectively. Compared with the spectra of clean Co(0001), the features are quite different; the results

are also unlike those of isolated graphene monolayers on oxide surfaces, which are relatively featureless[35].

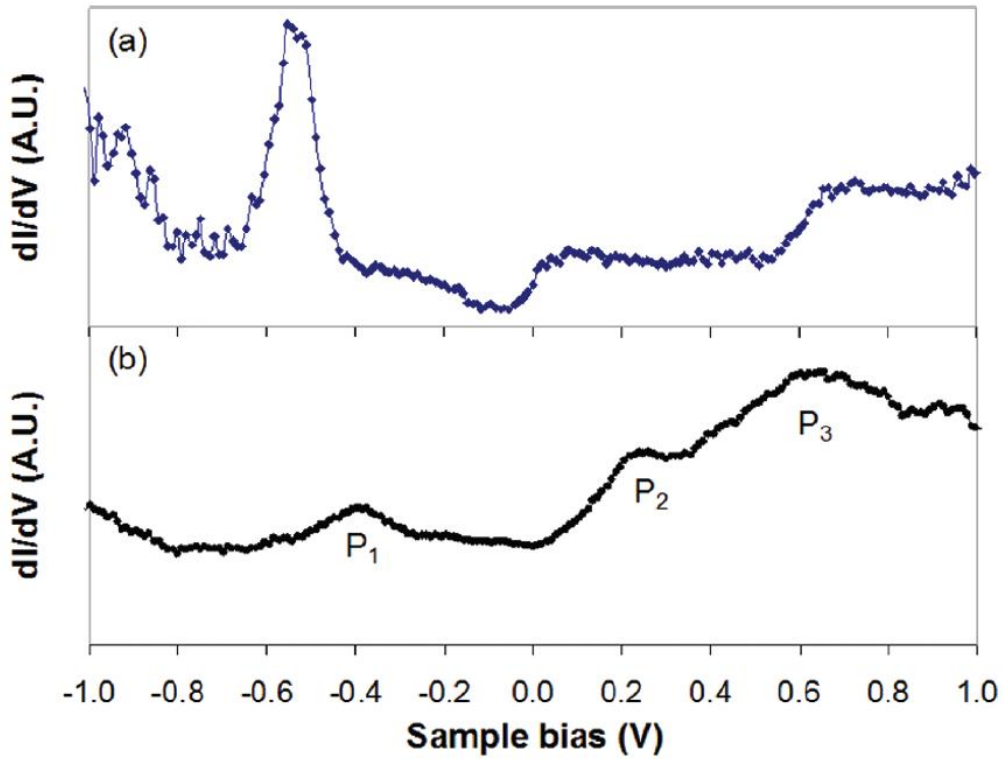

Figure 4.9: Experimental differential conductance spectra, dI/dV, of Co(0001) and graphene island/Co

Experimental differential conductance spectra, dI/dV, of (a) clean Co(0001) substrate and (b) graphene island on Co(0001), averaged over the rectangular region shown in Figure 4.7a. The three main features are labeled as P_1, P_2, and P_3, respectively. All energies are referenced to the Fermi level.

Since the AC structure is the most stable structure among the three possible structures, the band structure for AC is obtained by DFT calculation. In Figure 4.10, the majority-spin bands are shown in grey shade, among which the contributions from carbon are

shown in red dots. In order to compare with the ideal graphene sheet, we also plot the band structure of the ideal graphene sheet in the same figure in black lines, only with an energy downshift of 1.1eV. In the figure, we can find that the downshifted σ bands for ideal graphene sheet and graphene/Co perfectly overlap, as expected, because σ bonds are in-plane and don't interact with Co. The downshift of 1.1eV indicates an apparent n-dope situation. The calculated work function for graphene/Co is 3.65eV, while those for isolated graphene and Co(0001) are 4.39eV and 5.40eV, respectively. The decrease of the work function is consistent with the downshift of σ bands.

The π bands are very different between isolated graphene and graphene/Co. The Dirac cone of the ideal graphene at K point has been destroyed. The apparent portions of the π bands are shifted by an additional ~1eV. These observations indicate a strong coupling of the π bands to Co substrate.

The projected density of states (PDOS) of graphene/Co is calculated by summing up the projections of each state onto the carbon p_z orbitals. The upper majority-spin band in Figure 4.10b results in two peaks from -2V to 2V: 0.8eV and -0.3eV, which are derived from the carbon contributions from the region near M-K line. (The main contribution from carbon to the bands, shown in red dots in Figure 4.10 for the two spin channels (red dots), is mainly visible around the K point.) On the other hand, the minority-spin band in Figure 4.10c results in two analogue peaks at 1.7eV and 0.8eV.

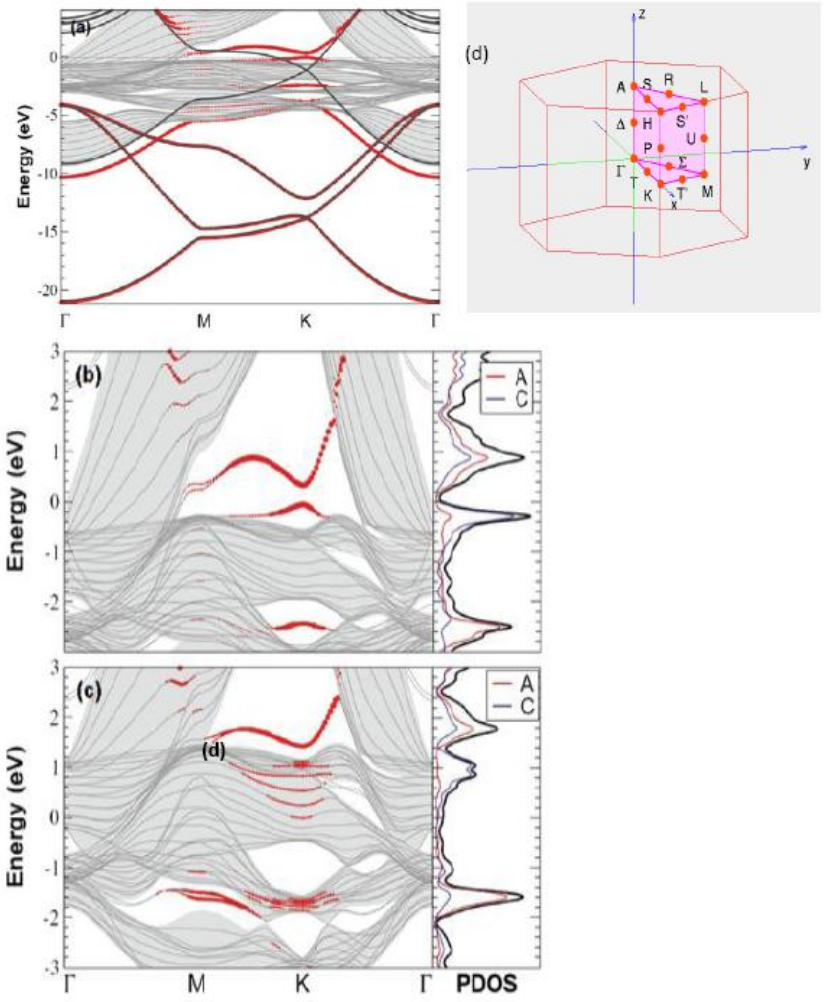

Figure 4.10: Calculated energy bands are density of states of graphene on Co(0001) in the AC geometry.

(a)Majority-spin bands with Co contributions (grey lines) and carbon contributions (red dots), against the bulk Co(0001) projected bands (shaded area) and the energy bands for ideal graphene downshifted by 1.1eV (black lines). (b) Details of (a) near Fermi level (on the left) and the atom-resolved and total projected DOS (on the right.) The red and blue curves are the PDOS from A-site and C-site, respectively. The black curve is the total PDOS. (c) Same of minority-spin bands.

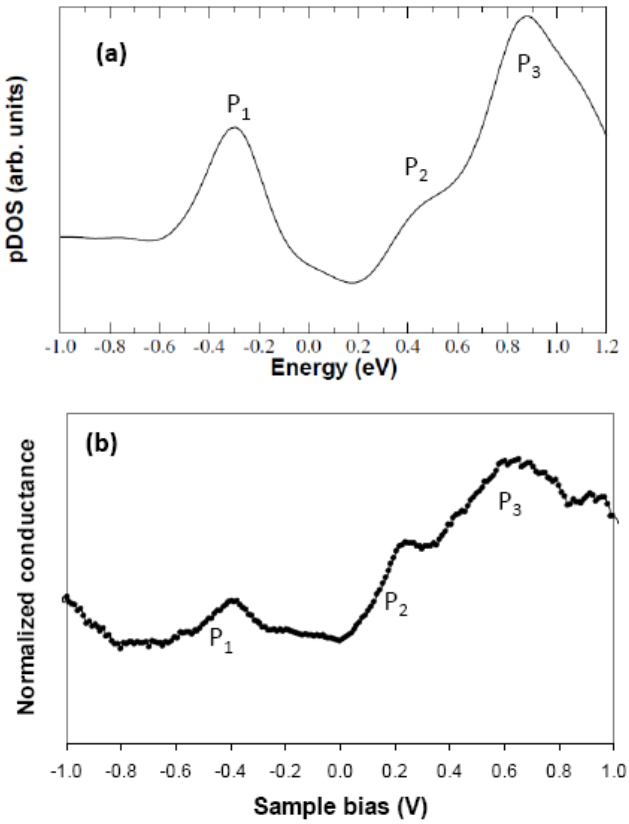

Figure 4.11: Comparison of calculated PDOS and experimental STS data of graphene/Co(0001).

(a) Calculated PDOS and (b) experimental STS data of graphene/Co(0001) with main features labeled with P_1, P_2, and P_3.

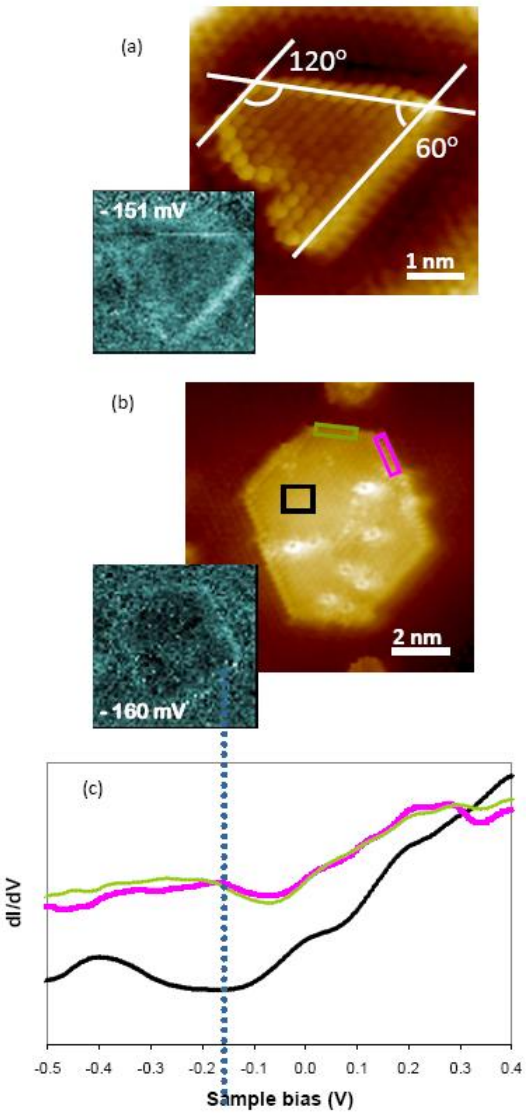

Figure 4.12: STM topographic images, conductance map, and STS of graphene islands on Co(0001).

(a-b) Topographic images of graphene islands with the corresponding conductance map around -150meV. The images were obtained at scanning bias of -3mV. (c) The STS of different regions on graphene islands. The pink and green curves were taken from edge regions and the black curve was from center region. The corresponding area is shown in (b) with the same colors.

The sum of the PDOS for majority-spin and minority-spin (shown in Figure 4.11a), which is consistent with the experimental results (shown again in Figure 4.11b), with differences in the feature locations of about 0.1-0.2eV. As noted above, those features result mainly from the regions near M-K line, which are expected to decay quickly as a function of distance above the surface near the Brillouin zone center. On the other hand, the states at zone center have little contribution from the graphene states, giving rise to featureless partial DOS, which is markedly different from the experiment. Therefore, we think that a mechanism which mixes zone-edge and zone-center states might be present.

4.3.3. Edge States

As mentioned above in Section 4.3.1, the graphene islands are mostly triangular or hexagonal, with angles either of 60^o or 120^o, preserving the edge type (See Figure 4.12a). In a closer inspection, we found that both of shapes have zigzag edges. In addition, we have found an edge localized state ~ -150meV if we compare STS in the center region with that of the edge region in Figure 4.12c. A conductance map around this bias also shows a bright feature localized at the edges (See insets of Figure 4.12a-b).

It is already known that armchair edge type was found to be more stable according to theory calculation[36]. However, in our calculation, when the ribbons are adsorbed to Co(0001) substrate, the zigzag type is found to be more stable, which is consistent with experimental results.

4.4. Summary

In conclusion, we have successfully grown epitaxial graphene nanoislands on Co(0001). Our STM results indicate an on-top registry with the underlying substrate with zigzag edges. These phenomena have been further validated by DFT calculations. We also observed several distinctive features from isolated graphene sheet in the conductance spectrum, which was interpreted to result from strong coupling with the cobalt substrate by DFT calculation. Furthermore, distinctive electronic features exist at the edges from center area, which will need further exploration.

4.5. Bibliography

1. Novoselov, K.S., et al., *Two-dimensional gas of massless Dirac fermions in graphene.* Nature, 2005. **438**(7065): p. 197-200.

2. Zhang, Y., et al., *Experimental observation of the quantum Hall effect and Berry's phase in graphene.* Nature, 2005. **438**(7065): p. 201-204.

3. Liu, L., et al., *Graphene Oxidation: Thickness-Dependent Etching and Strong Chemical Doping.* Nano Letters, 2008. **8**(7): p. 1965-1970.

4. Wehling, T.O., et al., *Molecular Doping of Graphene.* Nano Letters, 2007. **8**(1): p. 173-177.

5. Eom, D., et al., *Structure and Electronic Properties of Graphene Nanoislands on Co(0001).* Nano Letters, 2009. **9**(8): p. 2844-2848.

6. Cho, S., Y.F. Chen, and M.S. Fuhrer, *Gate-tunable graphene spin valve.* Applied Physics Letters, 2007. **91**(12).

7. Karpan, V.M., et al., *Graphite and Graphene as Perfect Spin Filters.* Physical Review Letters, 2007. **99**(17): p. 176602.

8. Ohishi, M., et al., *Spin injection into a graphene thin film at room temperature.* Japanese Journal of Applied Physics Part 2-Letters & Express Letters, 2007. **46**(25-28): p. L605-L607.

9. Mouras, S., et al., *Synthesis of first stage graphite intercalation compounds with fluorides*. Vol. 24. 1987, Paris, FRANCE: Gauthier-Villars.

10. Novoselov, K.S., et al., *Electric Field Effect in Atomically Thin Carbon Films.* Science, 2004. **306**(5696): p. 666-669.

11. Geim, A.K. and K.S. Novoselov, *The rise of graphene.* Nat Mater, 2007. **6**(3): p. 183-191.

12. Sutter, P., *Epitaxial graphene: How silicon leaves the scene.* Nat Mater, 2009. **8**(3): p. 171-172.

13. Chuhei, O. and N. Ayato, *Ultra-thin epitaxial films of graphite and hexagonal boron nitride on solid surfaces.* Journal of Physics: Condensed Matter, 1997. **9**(1): p. 1.

14. L. Zhao, K.T.R., H. Zhou, R. He, T. F. Heinz, A. Pinczuk, G. W. Flynn, A. N. Pasupathy, *The Atomic-scale Growth of Large-Area Monolayer Graphene on Single-Crystal Copper Substrates.* Arxiv.org, 2010.

15. *http://graphenetimes.com/1961/11/dunnste-kohlenstoff-folien/*.

16. Chen, J.-H., et al., *Intrinsic and extrinsic performance limits of graphene devices on SiO2.* Nat Nano, 2008. **3**(4): p. 206-209.

17. Morozov, S.V., et al., *Giant Intrinsic Carrier Mobilities in Graphene and Its Bilayer.* Physical Review Letters, 2008. **100**(1): p. 016602.

18. Tombros, N., et al., *Electronic spin transport and spin precession in single graphene layers at room temperature.* Nature, 2007. **448**(7153): p. 571-574.

19. Barone, V., O. Hod, and G.E. Scuseria, *Electronic Structure and Stability of Semiconducting Graphene Nanoribbons.* Nano Letters, 2006. **6**(12): p. 2748-2754.

20. Han, M.Y., et al., *Energy Band-Gap Engineering of Graphene Nanoribbons.* Physical Review Letters, 2007. **98**(20): p. 206805.

21. Okuno, S.N., T. Kishi, and K. Tanaka, *Spin-Polarized Tunneling Spectroscopy of Co(0001) Surface States.* Physical Review Letters, 2002. **88**(6): p. 066803.

22. Barral, M., et al., *Characterization of the surface states of Co(0001), Co(111), and ultrathin films of Co on Cu(111).* Physical Review B, 2005. **72**(12): p. 125433.

23. Math, C., J. Braun, and M. Donath, *Unoccupied spin-split surface state on Co(0001): experiment and theory.* Surface Science, 2001. **482-485**(Part 1): p. 556-561.

24. Erbudak, M., et al., *Surface Phase Transitions during Martensitic Transformations of Single-Crystal Co.* Physical Review Letters, 1997. **79**(10): p. 1893.

25. Wetli, E., et al., *High-resolution photoemission study of hcp-Co(0001).* Surface Science, 1998. **402-404**: p. 551-555.

26. Himpsel, F.J. and D.E. Eastman, *Intrinsic Lambda _{1}-symmetry surface state on Co(0001).* Physical Review B, 1979. **20**(8): p. 3217.

27. Georg Schmidt, R.F.T.G.G. and et al., *Electrical spin-injection into semiconductors-from cobalt contacts to semiconductor spin aligners*. 2000, Springer. p. 309-320.

28. *Wikipedia*. [cited 2010 12/09]; Available from: http://en.wikipedia.org/wiki/Cobalt.

29. Giber, J., R. Drube, and V. Dose, *Critical point energies in hcp and fcc cobalt from appearance potential spectra.* Applied Physics A: Materials Science & Processing, 1991. **52**(2): p. 167-170.

30.Lee, B.W., et al., *Surface structures of the two allotropic phases of cobalt.* Physical Review B, 1978. **17**(4): p. 1510.

31. Xiao, S., et al., *Molecular Wires from Contorted Aromatic Compounds.* Angewandte Chemie International Edition, 2005. **44**(45): p. 7390-7394.

32. Vaari, J., J. Lahtinen, and P. Hautojärvi, *The adsorption and decomposition of acetylene on clean and K-covered Co(0001).* Catalysis Letters, 1997. **44**(1): p. 43-49.

33. Gwo, S. and C.K. Shih, *Site-selective imaging in scanning tunneling microscopy of graphite: The nature of site asymmetry.* Physical Review B, 1993. **47**(19): p. 13059.

34. Giovannetti, G., et al., *Doping Graphene with Metal Contacts.* Physical Review Letters, 2008. **101**(2): p. 026803.

35. Stolyarova, E., *unpublished results.*

36. Wassmann, T., et al., *Structure, Stability, Edge States, and Aromaticity of Graphene Ribbons.* Physical Review Letters, 2008. **101**(9): p. 096402.